Chapter 1

Laser Welding of Magnesium Alloys: Issues and Remedies

Masoud Harooni and Radovan Kovacevic

Additional information is available at the end of the chapter

http://dx.doi.org/10.5772/66608

Abstract

Automotive industry tends to use lightweight alloys to save on mass in order to have more economic and environment friendly automobiles. A variety of alloys have been used in automotive industry such as magnesium, aluminum, and galvanized steel. Magnesium is the lightest structural metal that can significantly help decrease the body structure weight. Laser welding is one of the main joining processes used in automotive industry due to its superior joint properties. In the current study, the main issue that was pore formation during the laser welding of magnesium alloy is investigated. First, the process was performed using different process parameters to study their effect on the weld quality. Then a variety of approaches were used to mitigate pores in the weld. The results showed that these approaches could effectively mitigate pore formation in the weld bead. In addition, the pore formation issue was nondestructively detected using real-time methods such as spectrometer and high speed charge-coupled device (CCD) camera. The results showed that there was a good correlation between pore formation and the real-time-monitoring detected data.

Keywords: laser welding, magnesium alloy, porosity, spectrometer, online monitoring, numerical modeling

1. Introduction

One of the main concerns for the automotive industry is the CO_2 emission targets requested by governments globally. One reaction to this demand is a renewed focus on mass savings. Lightweight components improve human life quality by two aspects: providing more economic means of transportation and a cleaner environment due to less greenhouse gas generation [1, 2]. A mass reduction of 10% in an automobile will reduce 7% of the fuel consumption [3]. Magnesium is one of the most favorite selections for mass savings since it is the lightest structural metal and has the best strength-to-weight ratio among commercial metals. The density of magnesium is 36% less than aluminum and 78% less than steel. The production of magnesium increased by 390% from 1995 to 2007. This increase demonstrated the growing demand for magnesium in different industries [3]. Repots reveal that automotive industry achieved an average of 25% reduction in fuel consumption between 1990 and 2005 [4].

Magnesium alloy consumption takes different shapes and forms for different industries [1]. To satisfy the production of different shapes to fit industry needs, it is necessary to study the joining processes of this alloy [5]. Different joining processes such as laser welding [1, 6], arc welding [1], hybrid laser-arc welding [1, 7], friction stir welding (FSW) [1, 8], resistance spot welding [1, 9], and electromagnetic pulse welding [1, 10] are used for welding magnesium alloys. Among these processes, laser welding is paid more attention due to its advantages. High power density, low heat input, and consequently a narrow fusion zone and heat-affected zone (HAZ), a high depth-to-width ratio, and suitability for joining complex shapes are some of the advantages of laser welding [1]. Previous authors' studies on laser welding of magnesium alloys are summarized in **Table 1**.

Title	Ref.
Mitigation of pore generation in laser welding of magnesium alloy AZ31B in lap joint configuration	[11]
Studying the effect of laser welding parameters on the quality of Zek100 magnesium alloy sheets in lap joint configuration	[12]
Effect of process parameters on the weld quality in laser welding of AZ31B magnesium alloy in lap joint configuration	[13]
Dual-beam laser welding of AZ31B magnesium alloy in zero-gap lap joint configuration	[14]
Detection of defects in laser welding of AZ31B magnesium alloy in zero-gap lap joint configuration by a real-time spectroscopic analysis	[15]
Pore formation mechanism and its mitigation in laser welding of AZ31B magnesium alloy in lap joint configuration	[16]
Two-pass laser welding of AZ31B magnesium alloy	[17]
Experimental and numerical studies on the issues in laser welding of lightweight alloys in a zero-gap lap joint configuration	[18]

Table 1. Authors' previous studies on laser welding of magnesium alloys.

2. Joining of magnesium alloys

There are a variety of methods that has been used for joining of magnesium alloys. In the following section, a brief description of each method along with its advantages and disadvantages is discussed.

2.1. Adhesive bonding

This method employs adhesive to make a bonding between two parts. It usually can be used for any material and it is suitable for complex shape and size. However, the surface of the alloys should be treated before applying the adhesive. This is one of the disadvantages of this method. The treatment includes degrease, abrasion, and chemical methods [1]. Again, this will take time and needs an extra operation which is not desirable for production industry. After treatment, the adhesive should be applied evenly and sometime small plastic spheres are added to adhesive to assure the consistent gap between two parts.

After applying the adhesive on between two parts, it should be cured. The curing process could be performed in room temperature or by using heat [1]. This might take few minutes to several hours based on the type of the applied adhesive. This could be a time-consuming step that is not advantageous for industry. Overall, this method is desirable because it saves on mass for joining parts and also it does not melt the base metal. On the other hand, it is relatively long process and it is not suitable for mass production joining processes.

2.2. Frictions stir welding

This is a solid-state welding process that does not use heat source to melt the base metal. Instead, joining process is performed using a plastic deformation in the base metals. Generally, this process can be compared with forming manufacturing processes. This process was mainly applied for aluminum alloys at the beginning, but it was used for other alloys later. This method is a solid phase process; therefore, issues that occur during the fusion welding such as solidification cracking, distortion, spatter, and radiation are not a problem during the friction stir welding (FSW) [1]. Due to the same property of this method, the microstructure of the metal after FSW process have fine grains which results in a superior mechanical property. However, this method is not suitable for complex shapes and thin metal sheets that are commonly used in industry. This method also uses a tool which has a limited life and in comparison with laser welding which is noncontact is considered a more expensive process [1].

2.3. Resistance spot welding

This method is one of the main processes used in automotive industry to join metals, but it is not performed for magnesium alloys. This process is at the stage of research mainly but needs more work and efforts to get to production levels for this alloy. This method is considered one of the most economic processes in automotive industry to join sheet metal in body structure. The generated heat is based on the electrical resistance of the metal, and the process should be performed very fast to avoid heat dissipation in the whole part. This rapid local heat generation results in high solidification rate that finally produces dendritic microstructure [1]. Due to low corrosion resistance property in magnesium alloy, mainly a coating layer is used on the surface of the metal sheet. This layer is not conductive and should be removed prior to resistance spot welding [1]. In addition, magnesium is very reactive metal and can form oxide layer on its surface rapidly that will affect its weldability in this method. It should be noted that this method is suitable for complex shapes and geometries. It seems that this method is well developed for aluminum but requires more research on magnesium alloys.

2.4. Laser

Laser is a high intensity heat source that can be used for different processes such as cladding, welding, and heat treatment. Laser welding is one of the most efficient joining processes having high power density which is used to join similar and dissimilar materials. One of the main advantages of laser welding is the relatively high welding speed compared to other fusion welding processes. This helps industries to reduce their mass production cycle time. Heat input is one of the main causes of metallurgical issues in the welding of metals. This parameter shows that to achieve a nominal weld depth, how much heat should be inserted to the workpiece. Since laser has a high intensity (power/beam area at focus), a higher depth could be achieved using a lower heat input compared to other welding methods. As a result, the high depth-to-width ratio of the weld bead shape in laser welding introduces a better weld quality due to the limited size of the HAZ [18].

3. Issues in welding of magnesium and the suggested remedies

3.1. Porosity

Among a variety of issues in welding of magnesium alloys, porosity has a major effect upon the weld joint mechanical properties. There are several reasons for pore formation in the welding of magnesium alloys. Therefore, it is important to understand the pore formation mechanisms and their mitigation procedures during the welding process. Different mechanisms cause pore formation in the laser welding process, including hydrogen pores [1, 19], unstable keyhole [20], preexisting pores, surface coating [1, 15, 16], gas entrapment [1, 21], and alloy elements with a low vaporization point [22].

3.1.1. Hydrogen gas

The only gas that can be dissolved in molten magnesium is hydrogen [6]. Hydrogen pores are formed by the difference in solubility of hydrogen in solid and liquid magnesium. As molten magnesium solidifies, hydrogen solubility sharply decreases and rejects the hydrogen gas resulting in pore formation in the weld bead [1]. Mikucki and Shearouse [19] concluded that the hydrogen content should be kept as low as possible in magnesium in order to prevent pore formation during the solidification process [19].

3.1.2. Preexisting pores

Preexisting pores are another cause of pore formation in the weld bead of magnesium alloys [1, 6]. The initial high gas content in magnesium alloys is one of the reasons for pore formation in the weld bead, especially in alloys that are die-casted [6]. The welding procedure provides the condition for the pores to coalesce and form larger pores [1, 6, 23]. It is noted that a higher welding speed reduces the available time to form and grow pores, resulting in fewer pores in the weld bead [23].

3.1.3. Oxidation and surface coatings

Surface coatings could generate pores during the laser welding process. The results showed that the existing oxide layer on the surface of magnesium alloy is the main cause of porosity in laser-welded samples [11, 16]. It was concluded that the pore formation mechanism was due to magnesium hydroxide decomposition during the laser welding process.

3.1.4. Unstable keyhole

An unstable keyhole is one of the causes of pore formation in the laser welding process [6]. Keyhole stability depends on properties of the molten metal such as surface tension and vapor pressure [23]. The vapor pressure inside the keyhole forces the keyhole to be open, whereas surface tension tends to close the keyhole [23]. In laser welding of aluminum alloys, the keyhole oscillates and contributes to the pore formation [24]. However, magnesium has a much higher vapor pressure and lower surface tension than aluminum alloys [23] resulting in higher stability of keyhole during the laser welding process.

3.1.5. Gas entrapment

Gas entrapment in the molten pool is another reason for pore formation in the weld bead [6, 21]. Pores created by this mechanism are a result of the oscillation of the surface of the molten pool that entraps gases from the air [21]. The oscillation of the surface happens in the laser welding of magnesium because magnesium has an extremely low surface tension and viscosity [6]. In order to prevent gas entrapment in the laser welding of magnesium, it is suggested to use a shielding gas with the appropriate parameters [21].

3.2. Cracking

Cracking is another defect that is common in the welding of a magnesium alloy. Magnesium alloys are susceptible to two types of cracking during the welding process. Solidification cracking is one of them and the crack occurs during the solidification. The other one is liquation cracking which mainly occurs in heat affected zone (HAZ). Hot cracking (solidification cracking) is reported to be the main crack type in magnesium alloys [6]. The coefficient of thermal expansion for magnesium is high (twice that of steel). Therefore, during the welding process, thermal stress results in the deformation of magnesium sheets that finally cause cracking in the weld bead. Alloying elements in the magnesium alloy make the cracking even worse. Magnesium forms intermetallics with alloying constituents such as Mg-Cu, Mg-Al, and Mg-Ni. These intermetallics have a low melting point in comparison to the magnesium melting point. Therefore, these intermetallics remain liquid among the grain boundaries of solidified magnesium resulting in brittle boundaries that are susceptible to cracking [1]. In order to decrease cracking in the weld bead, different solutions such as back plating, adjusting the process parameters and the addition of alloying elements are suggested.

3.3. Oxidation

Magnesium is a very active material that can easily react with oxygen and be detrimental in the welding process. The magnesium oxide forms on the molten pool resulting in its irregular shape and low mechanical properties. Therefore, providing sufficient shielding gas during welding process is essential. In addition, magnesium has a low vaporization point that causes some of its loss during the welding process. The melting point and boiling temperature of magnesium are 630 and 1090°C resulting in a limited temperature range around 460°C. Therefore, it is necessary to employ a low heat input source that is easily controllable. One of the best choices is a laser beam heat source that has low heat input and also can be controlled. Another solution is to substitute the loss of material with the addition of alloying elements or fluxes in order to increase the vaporization point [1].

4. A variety of methods to mitigate porosity

In this section, a variety of methods are performed in order to mitigate pore formation caused by oxide layer existing on the surface of magnesium alloy AZ31B sheets. Magnesium is a very reactive alloy and oxidation is inevitable [1]. The oxide layer may form during the manufacturing process or even when the alloy is exposed to atmosphere. Magnesium has a low corrosion resistance and recently oxide-based coating is used to improve the corrosion resistance properties of this metal. AHC Surface Coating [25], Keronite [26], and Tagnite [27] are examples of coating processes that apply oxide-based coating on the surface of magnesium alloys. To satisfy the wide application of magnesium alloy in different industries, it has been necessary to develop a reliable joining process such as welding. Also, based on what was discussed about the existence of oxide layer on the surface of magnesium alloy, it seems necessary to investigate the effect of oxide layer on the weld quality. So far, there is no report on a cost-effective, efficient, and easy to-apply welding procedure that is capable of joining magnesium alloys sheets without removing the oxide layer prior to welding. In this chapter, a variety of methods are introduced to mitigate pore formation caused by oxide layer. In addition, prior to using these methods to mitigate pore formation, authors studied the effect of laser parameters on the pore formation in another work which is not presented at this work [13].

4.1. Mitigation of pore formation using a plasma arc preheating

For evaluating the influence of the oxide layer on the weld quality, three different surface conditions are introduced: as-received (AR) with the oxide layer remaining on the surface, mechanical removal (MR) of oxides by sand paper, and a heat-treated surface by plasma arc

(PA). In addition, in a separate experiment, a furnace is employed to compare results with the plasma arc preheating process. The results are discussed in detail in the following section.

4.1.1. Experimental setup

The laser welding experiments are performed using a 4-kW fiber laser. The experimental setup including a six-axis robot and a welding laser head is shown by the schematic view in **Figure 1**. As it is shown, a preheating source is used 100 mm prior to laser head. The nominal chemical composition of this alloy is shown in **Table 2**. Pure argon with a flow rate of 60 standard cubic feet per hour (SCFH) is employed to shield the molten pool. In all experiments, the focused laser beam with a beam diameter of 0.6 mm is set up on the top surface of the overlapped sheets to perform the laser welding process.

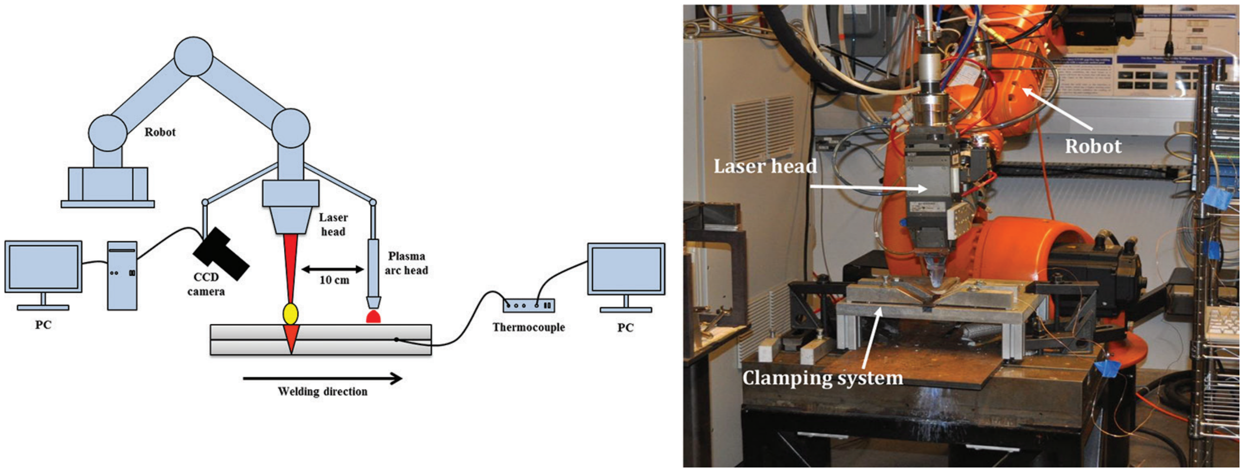

Figure 1. The schematic view of the experimental setup.

Element	Al	Zn	Mn	Si	Fe	Cu	Ni	Mg
Wt.%	2.46	1.70	0.58	<0.1	<0.005	<0.05	<0.005	Bal.

Table 2. The nominal chemical composition of the AZ31B magnesium alloy.

4.1.2. Experimental results

Figure 2 shows the AR samples cross-sectional views. It should be noted that the generated pores in the AR samples are mainly emanating from the faying surface of the two overlapped metal sheets. The presence of pores and also the arrangement of pores in the AR samples imply only that the source of pore generation might be the existing oxide layer on the surface of the AZ31B magnesium alloy sheet. That the oxide layer causes pore formation in the weld is also reported in literature [1, 6, 28, 29], however, without any discussion on how to mitigate its effect.

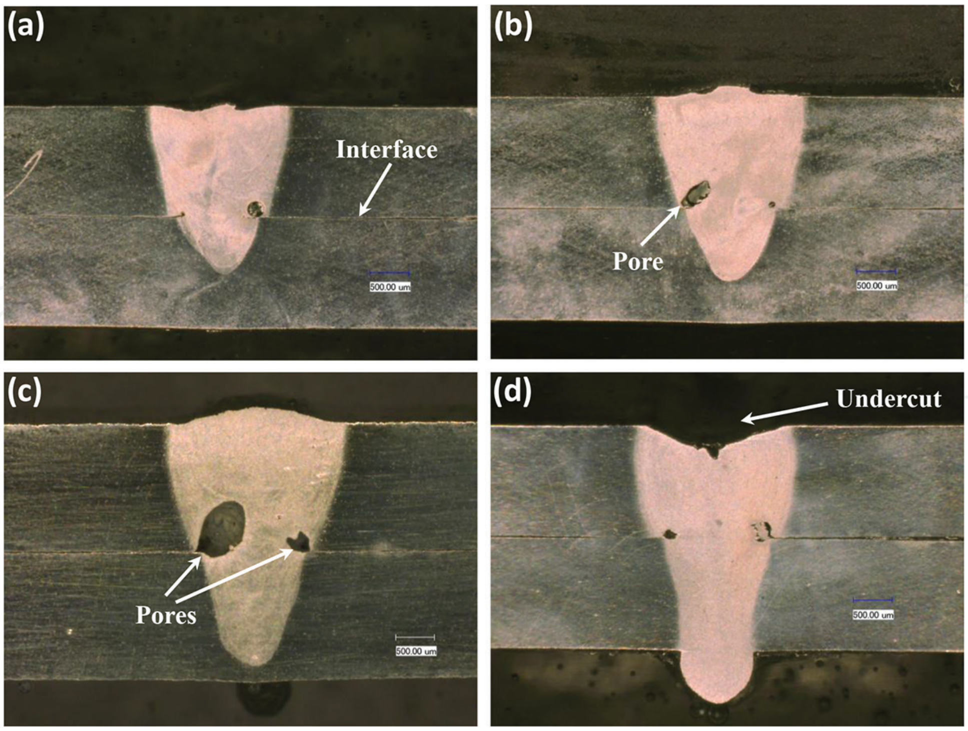

Figure 2. Weld cross-sectional views of AR samples with different laser powers (a) 800 W, (b) 900 W, (c) 1000 W, and (d) 1100 W.

In order to identify the oxide layer on the surface of the AZ31B magnesium alloy, energy-dispersive X-ray spectroscopy (EDS) analysis is applied for the AR and MR samples. The results of EDS are shown in **Figure 3(a)** and **(b)**. Considering these figures, the decrease in oxygen level is clearly shown on the surface of the MR-treated sample. The result denotes that the oxide layer on the AR sample is a dense oxide layer. Magnesium begins to oxidize around 450°C [6], and the oxide layer on AZ31B-H24 is formed by hot rolling process during the manufacturing process [30].

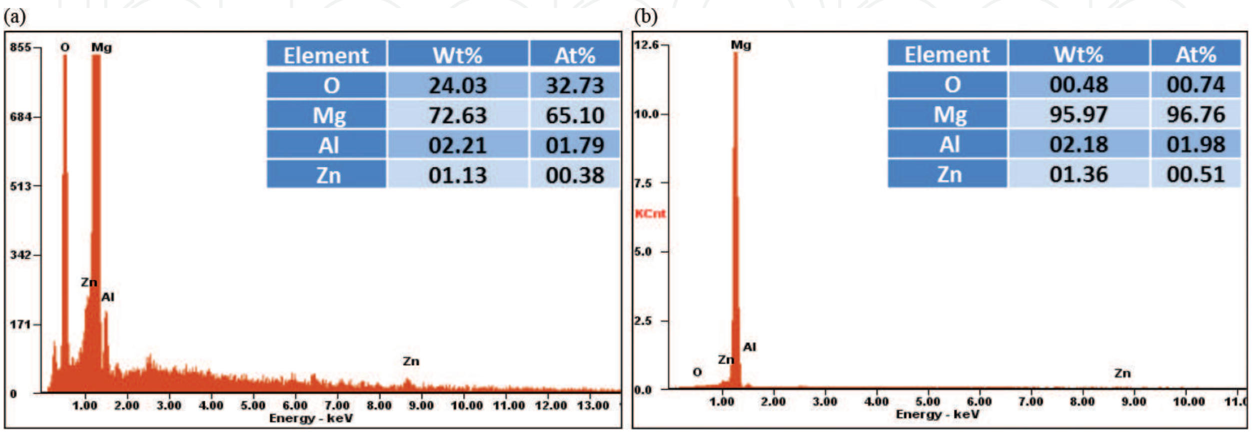

Figure 3. EDS results of (a) as-received and (b) mechanically removed samples.

http://dx.doi.org/10.5772/66608

The properties of oxide formed on metals are divided in two groups including protective and non-protective coatings [1, 31]. This category is based on the Pilling-Bedworth ratio (P-B ratio) R that is defined by the ($R = Wd/wD$) formula. Where W is the molecular weight of oxide, w is the molecular weight of metal, D is the density of oxide, and d is the density of metal [1, 31]. Pilling and Bedworth perceived that for R less than 1, the oxide layer on the metal is porous and non-protective [1]. As an example, aluminum and magnesium oxides are compared. The P-B ratio of Al_2O_3/Al is 1.280 and it is well accepted that aluminum oxide is a protective layer on the surface. On the other hand, the P-B ratio for MgO/Mg is 0.806, less than 1 [1]. Therefore, magnesium oxide is categorized under the porous and a non-protective group that easily forms the non-protective, porous, and thick oxide layer [1]. In order to clarify the P-B ratio effect on the oxide layer formation, a schematic view is presented in **Figure 4** [1].

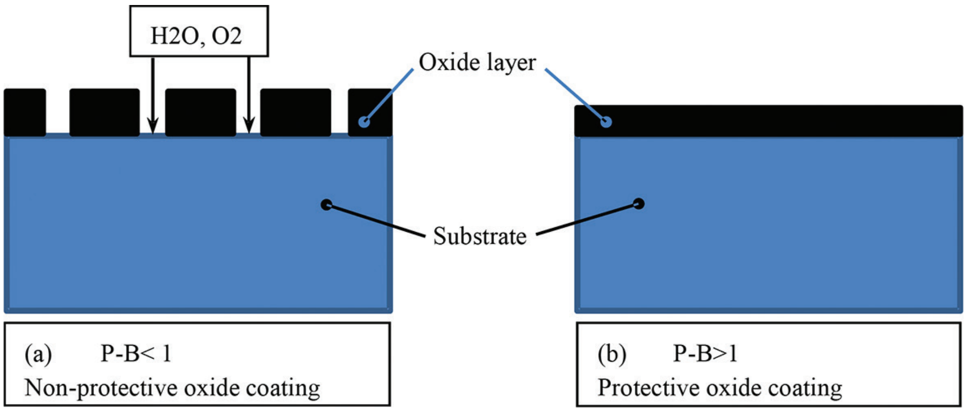

Figure 4. Schematic presentation of surface oxide formation on (a) magnesium alloy and (b) aluminum alloy [1].

The cross-sectional views of MR-treated samples are shown in **Figure 5**. The results show that by removing the oxide layer from the surface of the AZ31B magnesium alloy, pore formation is mitigated at the interface of the two overlapped metal sheets. This result implies that the source of pore formation is related to the oxide layer existing on the surface of the AZ31B magnesium alloy, as assumed.

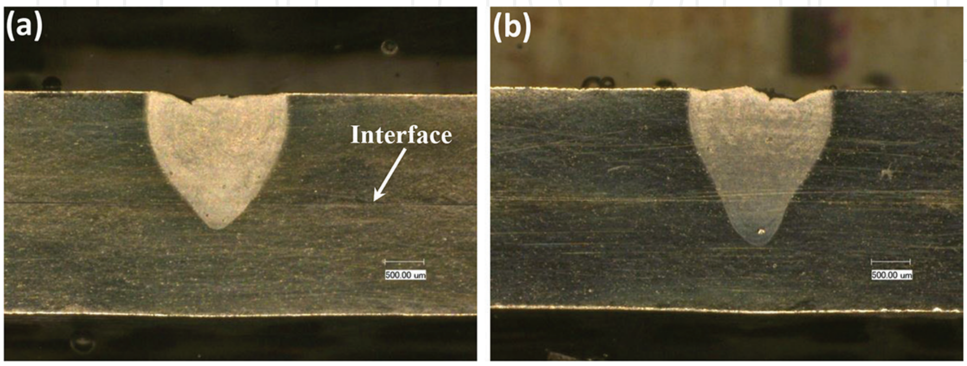

Figure 5. Welds cross-sectional views of MR-treated samples: (a) 1000 W and (b) 1100 W.

PA-treated samples cross-sectional views are illustrated in **Figure 6**. The results show that pores are effectively mitigated at the interface of the two overlapped metal sheets. Preheating the samples results in a change in the oxide layer and indirectly mitigates the pore formation in the weld bead.

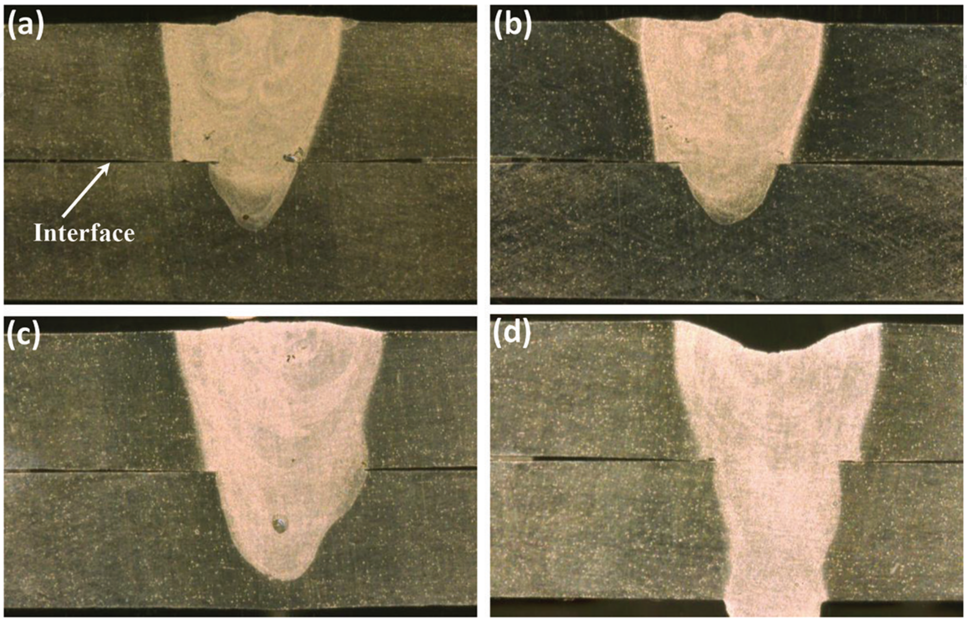

Figure 6. Welds cross-sectional views of PA-treated samples with different laser powers: (a) 800 W, (b) 900 W, (c) 1000 W, and (d) 1100 W.

Magnesium oxide is categorized under porous metal oxides by the P-B ratio and absorbs moisture from the air [6, 29, 32–35] as we discussed earlier in this section. Due to P-B ratio [1], magnesium is categorized under the alloys that form a nonprotective oxide layer on its surface. When magnesium is in atmosphere with moisture, magnesium hydroxide ($Mg(OH)_2$) is formed [6, 36, 37], as shown in Eq. (1). The decomposition temperature of magnesium hydroxide is about 200°C [36]. The water molecules will be released from magnesium hydroxide at this temperature [38]. The released water molecules have no escape path through the overlapped sheets. Instead, the water vapor escapes through the molten pool, resulting in pore formation inside the weld bead in the AR samples. In the PA-treated samples, preheating is performed prior to laser welding in order to decompose the magnesium hydroxide. Water molecules are then vaporized prior to laser welding at the faying surface of the two overlapped sheets. The stable keyhole in the laser welding acts as a chimney to vent the vaporized water to the atmosphere. Therefore, fewer pores are generated in the weld bead.

$$Mg\,(OH)_2 \rightleftarrows MgO + H_2O \tag{1}$$

To compare the surface chemical composition of AR and PA-treated samples, an XPS test was performed on the surface of both samples. The XPS survey spectra provided qualitative and quantitative surface composition information on samples of the AR- and PA-treated samples.

The primary detected elemental components in both cases are Mg, O, and C. The XPS spectrums of the two cases are shown in **Figure 7**.

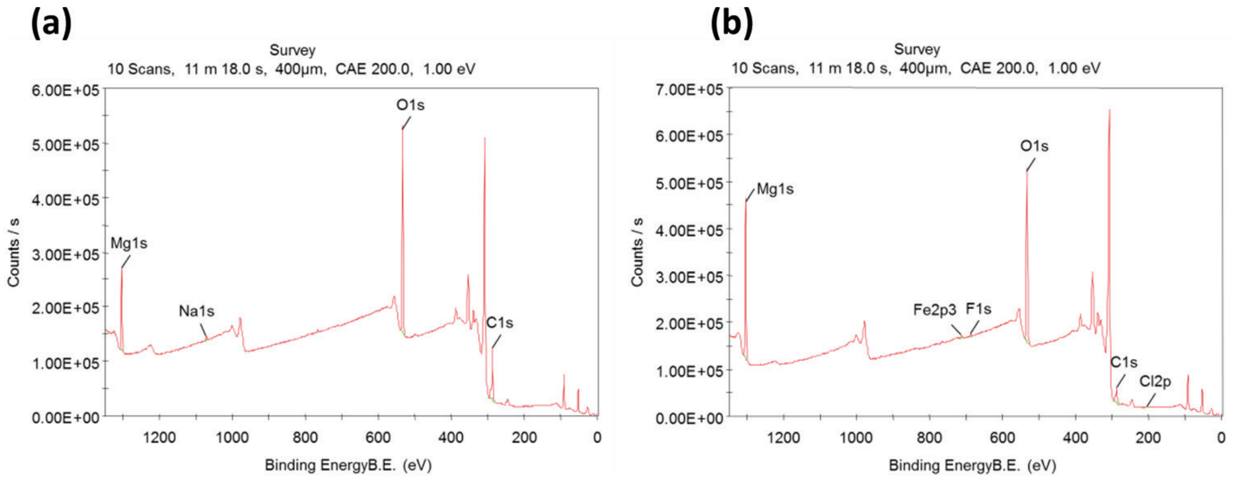

Figure 7. The XPS spectrum of the different cases: (a) AR sample, and (b) PA-treated sample.

The corresponding XPS surface composition results of AR and heat-treated samples are shown in **Table 3**. To quantitatively verify the oxide layer, the O/Mg surface atomic ratios are calculated from the XPS results. The stoichiometric surface composition of the AR sample is characteristic of $Mg(OH)_2$ (AR sample is 1.98, and $Mg(OH)_2$ [theoretical] is 2.00). The stoichiometric surface composition of the heat-treated sample is characteristic of MgO on its surface (PA-treated sample is 0.99, and MgO [theoretical] is 1.00). The above results indicate that the heat treatment converted the original $Mg(OH)_2$ surface layer to MgO on the as-received sample.

Sample	C	O	F	Na	Mg	Fe
AR	29.7	46.3	–	0.6	23.4	–
Heat-treated	11.5	43.6	0.3	–	44.0	0.3

Table 3. XPS survey spectra results (at.%).

The detection of hydrogen on the surface of AR and heat-treated magnesium alloy is not possible using the XPS or EDS methods due to atomic mass of this element. Reflected electron energy loss spectroscopy (REELS) testing is performed in order to quantitatively detect hydrogen on the surface of the AR and heat-treated samples. The results are shown in **Figure 8**. In **Figure 8**, the main peaks in the REELS spectra for the two samples are normalized to the same maximum intensity. Therefore, the observed differences in the intensity of the shoulders due to hydrogen on the main peaks illustrate true quantitative differences in the amount of surface hydrogen on the two samples. REELS confirmed the presence of hydrogen, presumably as $Mg(OH)_2$, on the surface of both samples. REELS indicated that the as-received sample had more hydrogen present compared to the heated sample, which is consistent with the XPS results, indicating the presence of primarily $Mg(OH)_2$ on the AR sample and $Mg(OH)_2$ plus MgO on the heated sample. This is discussed in more detail in authors' previous work [16].

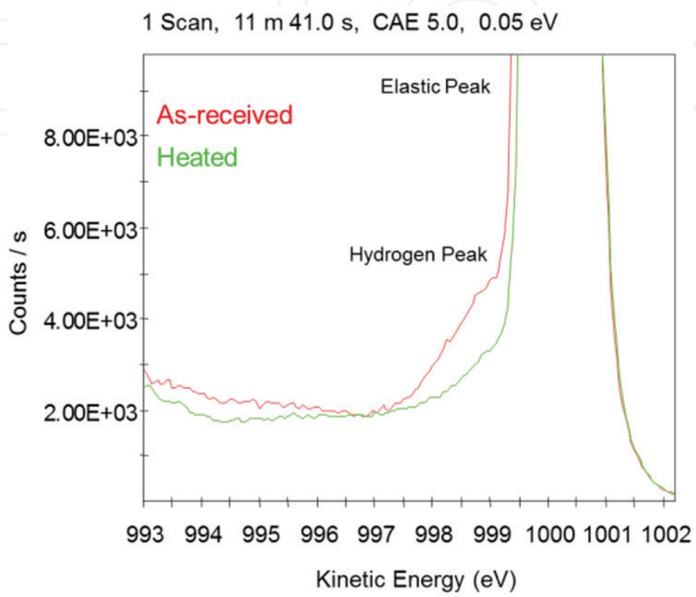

Figure 8. The comparison of REELS spectra for AR sample and heat-treated sample.

To verify if the preheating process provide sufficient temperature and width, a 3D model was developed. A heat source model for the plasma arc is the surface heat flux with a Gaussian distribution [39] and the material properties considered temperature dependent [18]. **Figure 9** shows the 3D view of the temperature field obtained by the numerical model in the plasma arc preheating procedure. It is good to check the isotherm of 200°C (minimum temperature for decomposition of magnesium hydroxide) for the two overlapped sheets. It is shown that the isotherm of 200°C reaches the interface of the two overlapped sheets.

Figure 10 shows the temperature history at the faying surface of the two overlapped sheets. The isotherm of 200°C shows that a width of 3.4 mm (1.7 mm each side) was preheated at the interface. Based on the experimental results achieved in Chapter 2, the maximum width of the weld pool at the faying surface of the two overlapped sheets in laser welding is 1.75 mm. This confirms that the preheated area reaching the temperature of 200°C could cover almost two times the width that is required.

The corresponding tensile test results are presented in **Figure 11** showing that the average tensile-shear loads of PA-treated samples are greater than those of the AR- and MR-treated samples. This is resulted from a lower level of pores in PA-treated samples. The weld bead tensile-shear load improves by 19% with PA-treated samples.

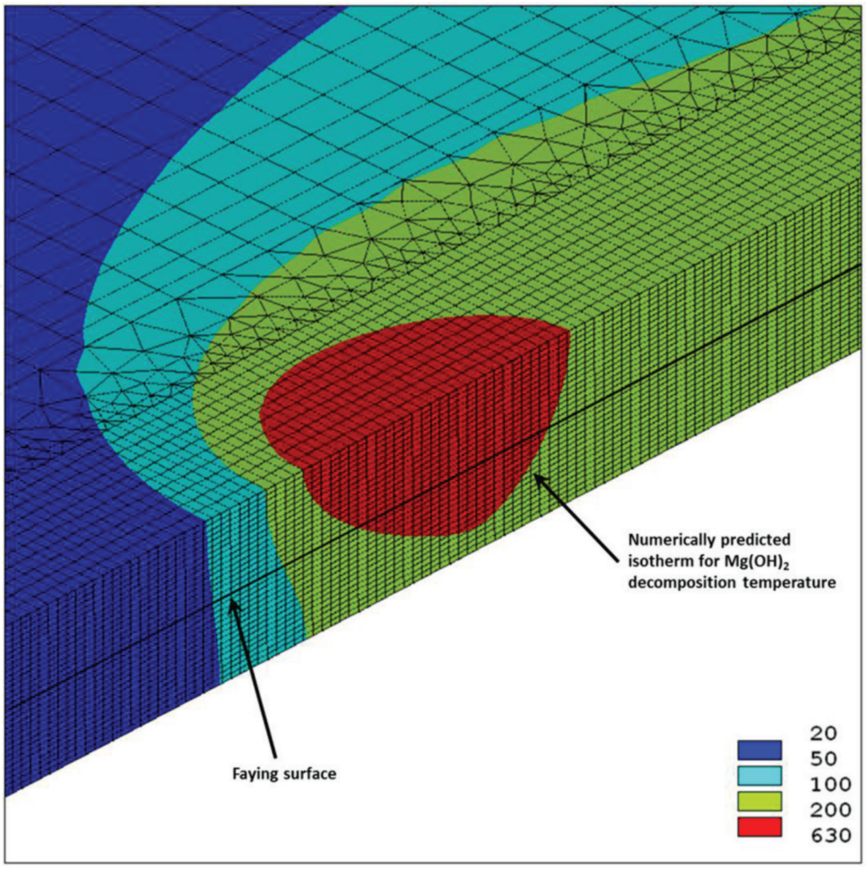

Figure 9. 3D view of temperature history in two overlapped sheets with a plasma arc preheating process with scanning speed of 30 mm/s.

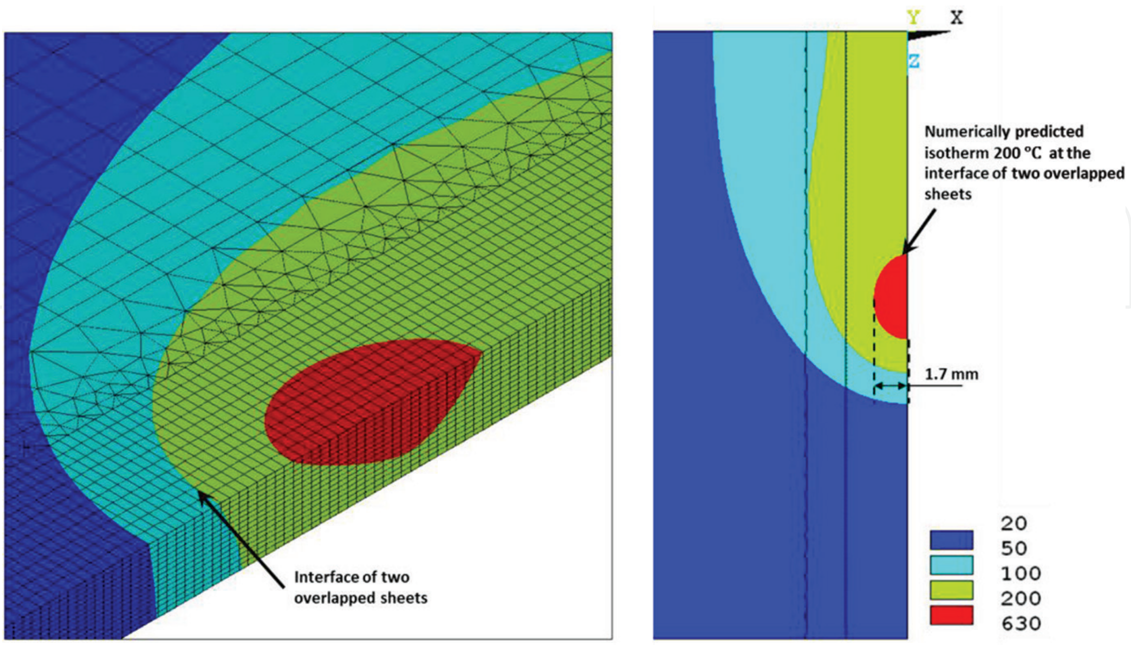

Figure 10. The temperature history of the preheating process at the interface of two overlapped sheets.

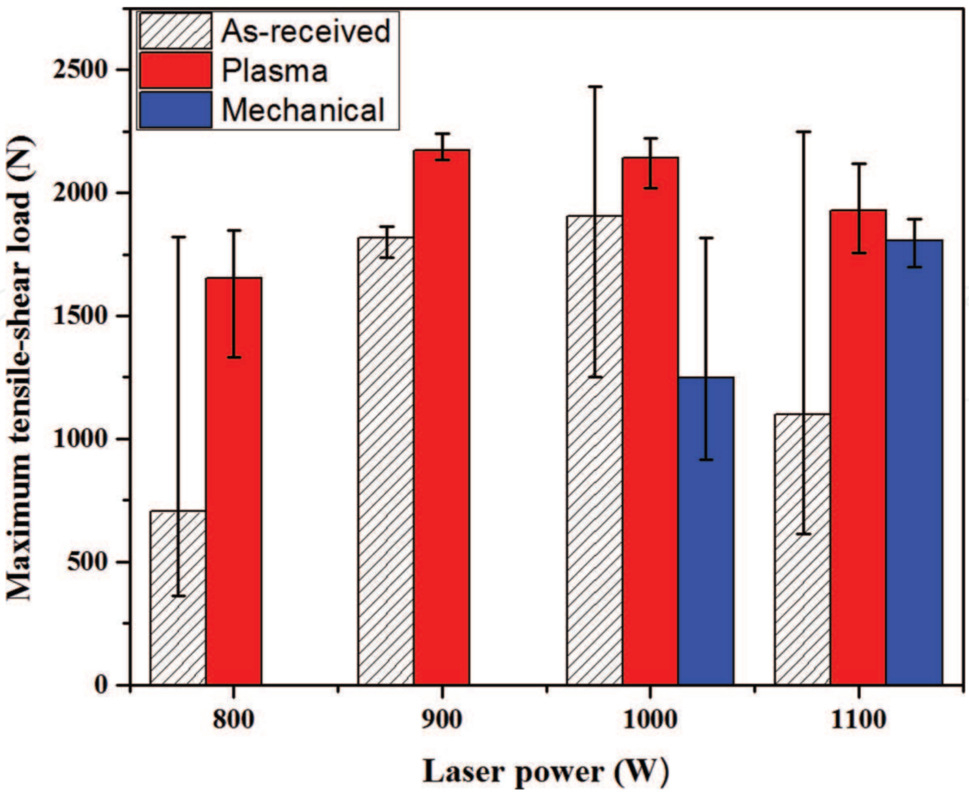

Figure 11. Tensile test results of laser welding AZ31B magnesium alloy.

4.2. Dual-beam laser welding of magnesium alloy

4.2.1. Experimental setup

In order to join AZ31B magnesium sheets in a lap joint configuration, a dual-beam laser was used to weld overlap samples. The single laser beam was changed to a dual-beam laser by using an optical prism as seen in **Figure 12**. An optical prism can divide the single laser beam into two separate spots. The distance between the two split beams was 0.6 mm, and the ratio of the laser power for each of the spots could be adjusted.

4.2.2. Experimental results

Figure 13 presents the profiles of the weld bead obtained during the laser welding process with two beam configurations. It is shown that the surface quality of the weld bead with dual-beam laser is smoother than the top surface of the weld bead obtained by a single laser beam. The improvement of surface quality could be described by a nondimensional hydrodynamic Froude number as a ratio of dynamic force to gravitational force expressed by Eq. (2) [41]:

$$F_r = \frac{V^2}{lg} \tag{2}$$

where V is welding speed, g is gravitational acceleration, and l is the characteristic length of the molten pool. Lower values of the Froude number corresponds to the improved quality of the surface [41]. By having two in-line laser spots in dual-beam laser welding, the length of the molten pool increases, and as a result, the Froude number decreases; that is, the top surface of the weld bead improves. An increase in the welding speed increases the Froude number resulting in a reduction of quality of the top surface of the weld bead, as confirmed by the authors in their earlier work [12].

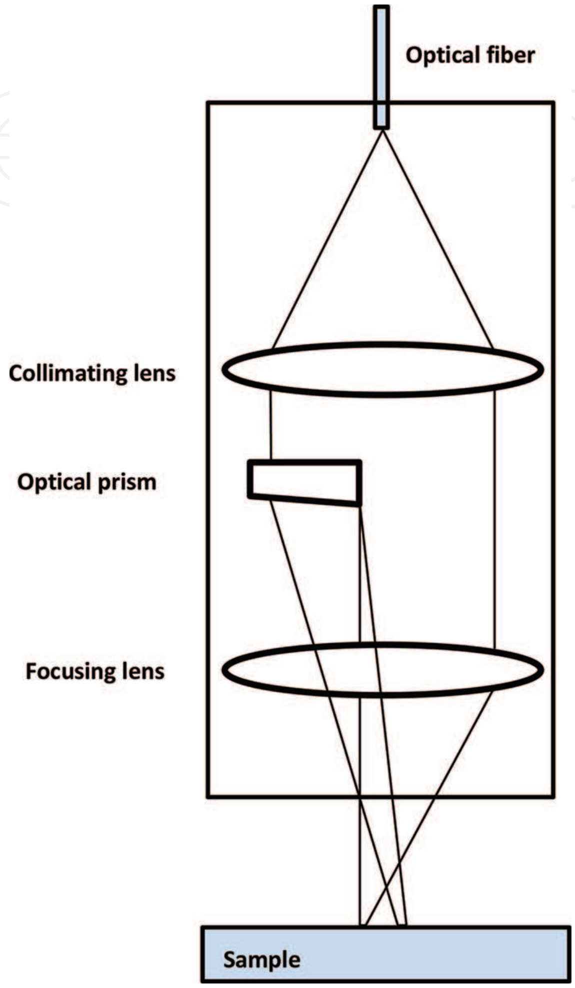

Figure 12. Schematic view of a dual-beam fiber laser head [40].

Four different beam energy ratios were chosen in combination with two laser power and welding speed settings and the results compared to those from a single beam in order to evaluate the effect of the split beam configuration. The baseline cross-sections from a single-beam exhibited pores emanating from the faying interface for both combinations of laser power and welding speed, refer to **Figure 14(i)–(j)**. Introducing the split beam at relatively high ratios of lead to lag beams for process conditions of 900 W at 30 mm/s and 1000 W at 50 mm/s also exhibited pore formation emanating from the faying interface in the weld cross-section; refer to **Figure 14(a)(c)** and **(e)(g)**, respectively. Not until the ratio was reduced to 20:80 was the pore formation at the faying interface of the weld cross-section effectively mitigated; refer to **Figure 14(d)** and **(h)**, for process conditions of 900 W at 30 mm/s and 1000 W at 50 mm/s, respectively. Thus, a split beam ratio of 20:80 for the leading beam power to lagging beam power appears to be an optimum for mitigating pore formation at the faying interface.

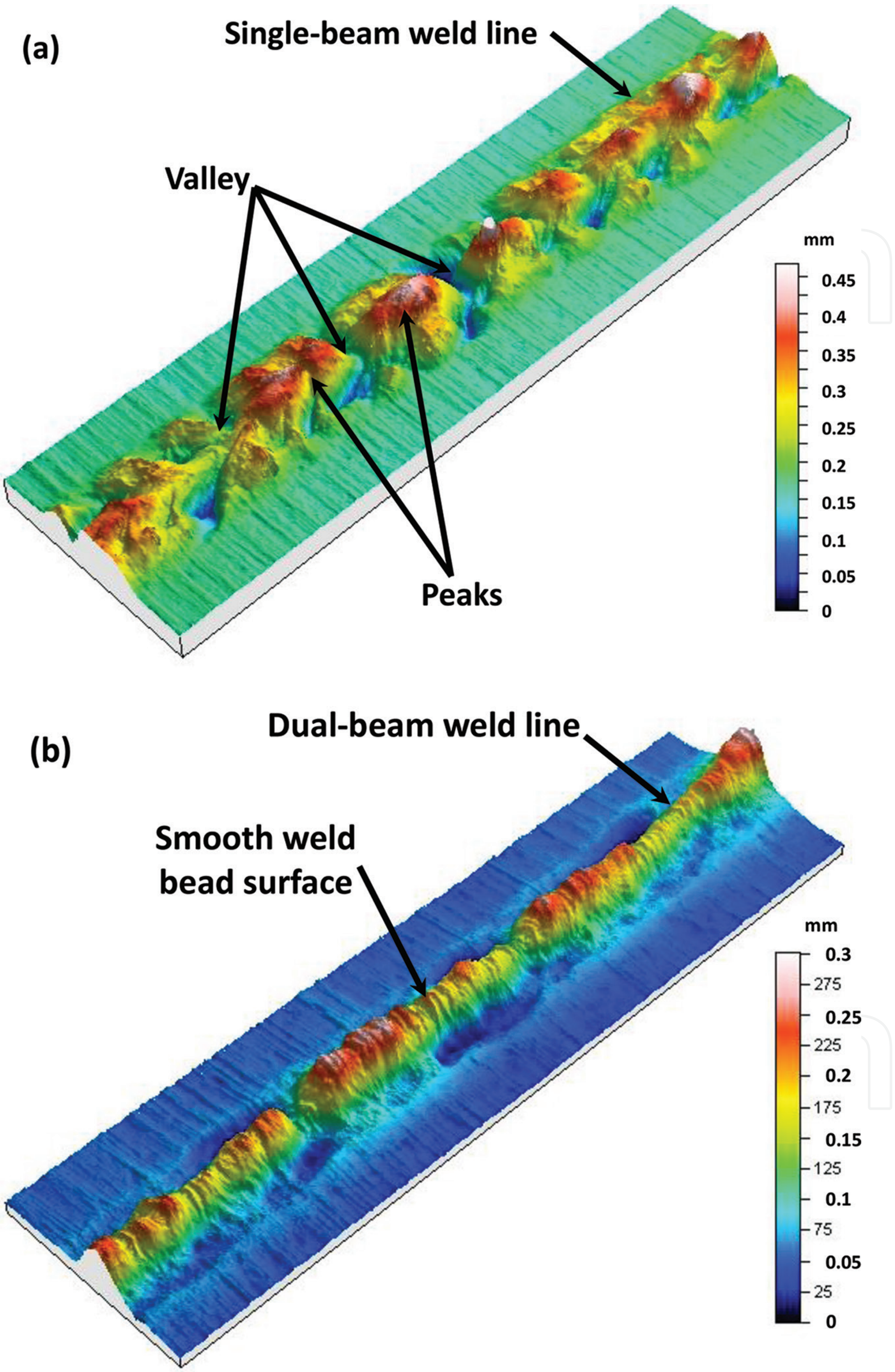

Figure 13. The profiles of the weld bead achieved under a welding speed of 30 mm/s and a laser power of 1000 W with (a) single-beam laser, and (b) dual-beam laser with a 20:80 split beam energy ratio [14].

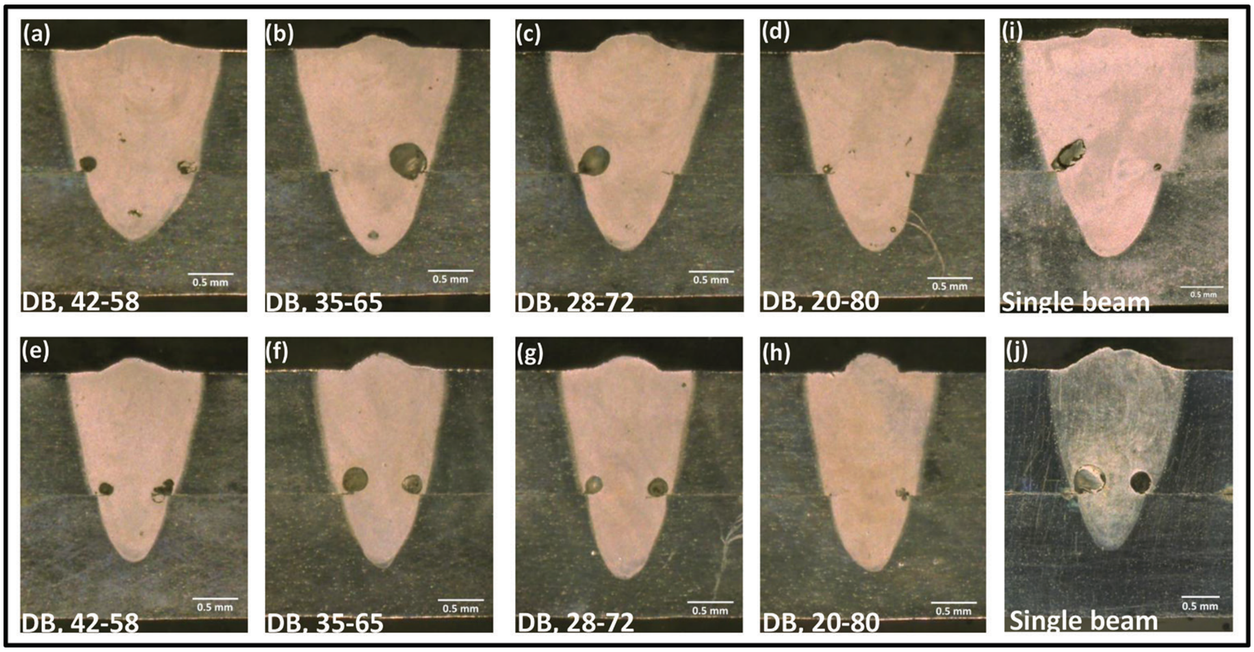

Figure 14. Cross-sectional views of the welds with a different beam ratios and laser process parameters (a)–(d) and (i) P= 900 W, V= 30 mm/s, (e)–(h) and (j) P = 1000 W, V = 50 mm/s.

As shown in **Figure 14**, pores are mitigated by a dual-beam laser for only an optimized beam ratio which indicates that there may be another mechanism involved in the mitigation of pore formation besides increasing of the molten pool size. As discussed previously, when the lead beam contains 20% of the laser power for preheating, the remaining 80% of laser power is used for welding and is sufficient to form a stable keyhole. The stable keyhole then serves as a chimney to vent the hydrogen gas from the decomposed magnesium hydroxide as shown in **Figure 15**. For the other beam ratios, the lead beam provides more than enough energy to preheat the sample; however, the lag beam is not able to form a stable keyhole thus increasing the probability of the hydrogen gas to be entrapped in the solidified weld pool. Thus, two mechanisms are necessary in order to achieve a high-quality weld. The first is the preheating procedure to decompose the magnesium hydroxide accomplished by the lead beam prior to laser welding. The second is the formation of a stable keyhole to vent the hydrogen gas during laser welding by the lagging beam. With a beam ratio of 20:80, the preheating procedure and formation of a stable keyhole provide an optimal distribution of heat resulting in a high-quality weld. **Figure 15** shows the schematic view illustrating the mechanism that mitigates pore formation in the weld bead during dual-beam laser welding.

In order to study the dynamic behavior of the weld pool, a high-speed CCD camera assisted with a green laser as an illumination source is used. **Figure 16** is composed of weld pool images captured by a CCD camera during the laser welding of AZ31B magnesium alloy with a laser power of 1000 W and welding speed of 30 mm/s with both single-beam and dual-beam laser configurations. No keyhole formation is observed during the single-beam laser welding process resulting in an unstable welding process refer to **Figure 16(a)** and **(b)**. In contrast, the images of the dual-beam laser weld pools exhibit a keyhole refer to the shiny dot at the center of the molten pool in **Figure 16(c)** and **(d)**. Although there was some instability in the formation of the keyhole during dual-beam laser welding, the instability was significantly less than for the case of single-beam laser welding. When the single-beam is used, the magnesium hydroxide decomposes and releases the water vapor into the molten pool resulting in collapse of the keyhole, turbulent flow in the molten pool, and porosity in the solidified weld. However, in the case of applying the dual-beam laser welding, the lead beam preheats the interface of the two overlapped sheets resulting in decomposition of the magnesium hydroxide. The lag beam with sufficient laser power then generates a stable keyhole, shown in **Figure 16(c)** and **(d)**, leading to mitigation of porosity.

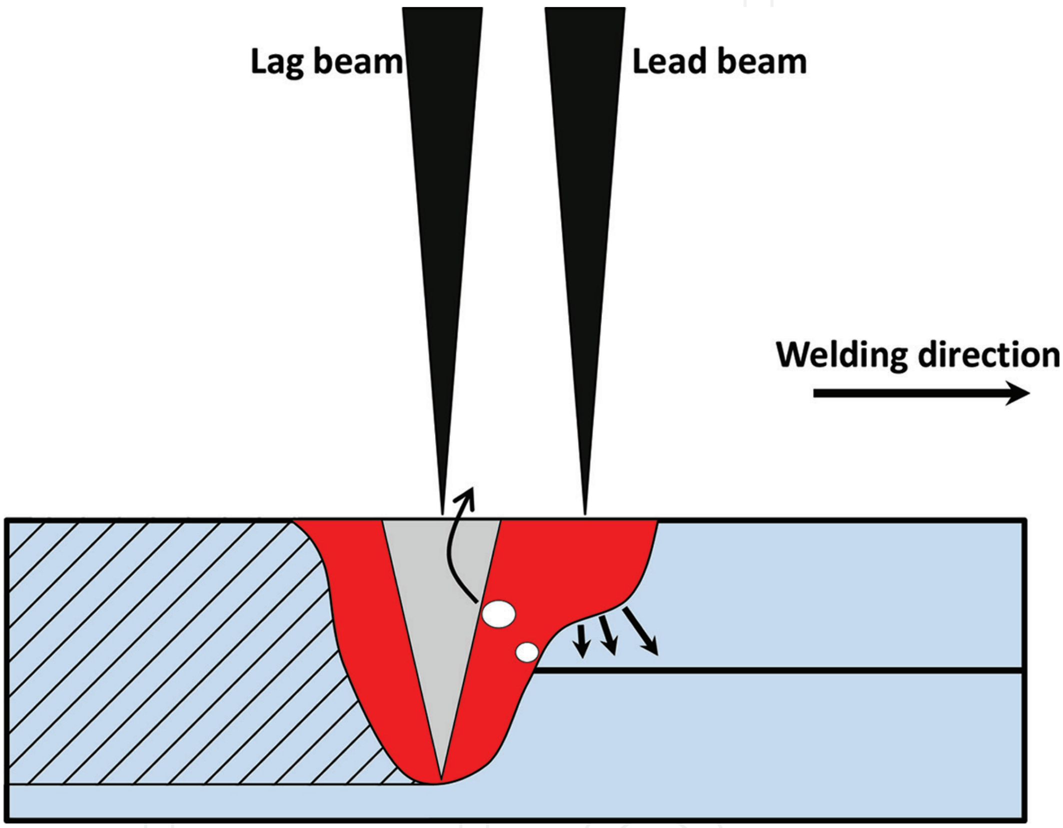

Figure 15. The pore formation mitigation mechanism during the dual-beam laser welding process.

Figure 17 presents the images of the laser-induced plasma plume captured during the laser welding of an AZ31B magnesium alloy with single-beam and dual-beam laser configurations. It is found that the plasma plume is more stable during the dual-beam laser welding process. **Figure 17(a)** presents the images of the plasma plume in the single-beam laser welding process. It is shown that the plasma plume is not stable and fluctuates during the laser welding process caused by water vapor at the faying surface of the two overlapped sheets. The plasma plume was extinguished during the welding process caused by the collapse of the unstable keyhole. The images of the plasma plume captured during the dual-beam laser welding (**Figure 17(b)**) show that the plasma plume exhibited greater stability than that obtained by single-beam laser welding. This is also reported by Xie [42].

http://dx.doi.org/10.5772/66608

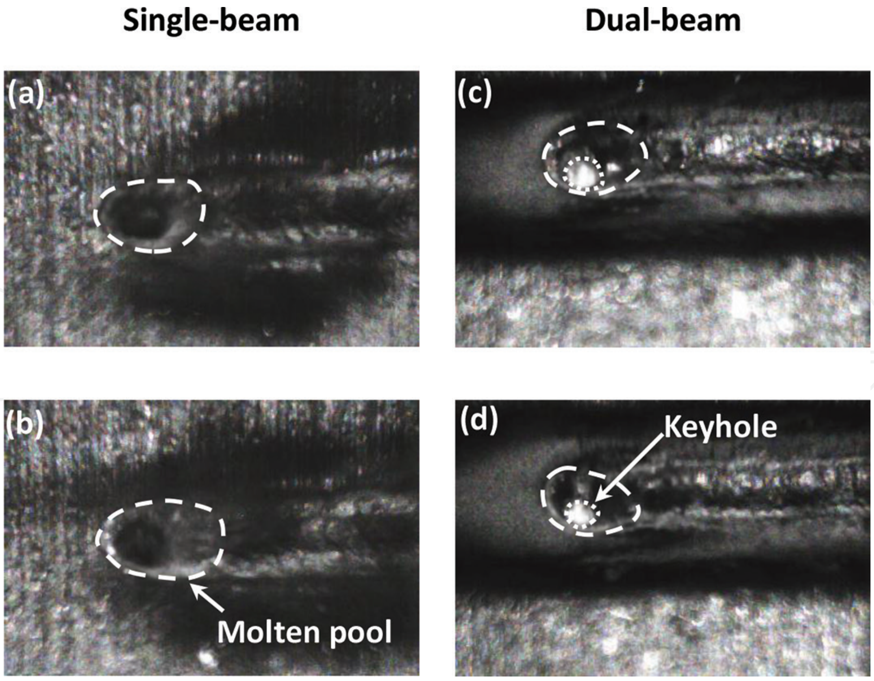

Figure 16. Images of the weld pool obtained with CCD camera with the laser power of 1000 W and welding speed of 30 mm/s (a), (b) single-beam, and (c), (d) dual-beam (lead/lag beam power ratio 20:80).

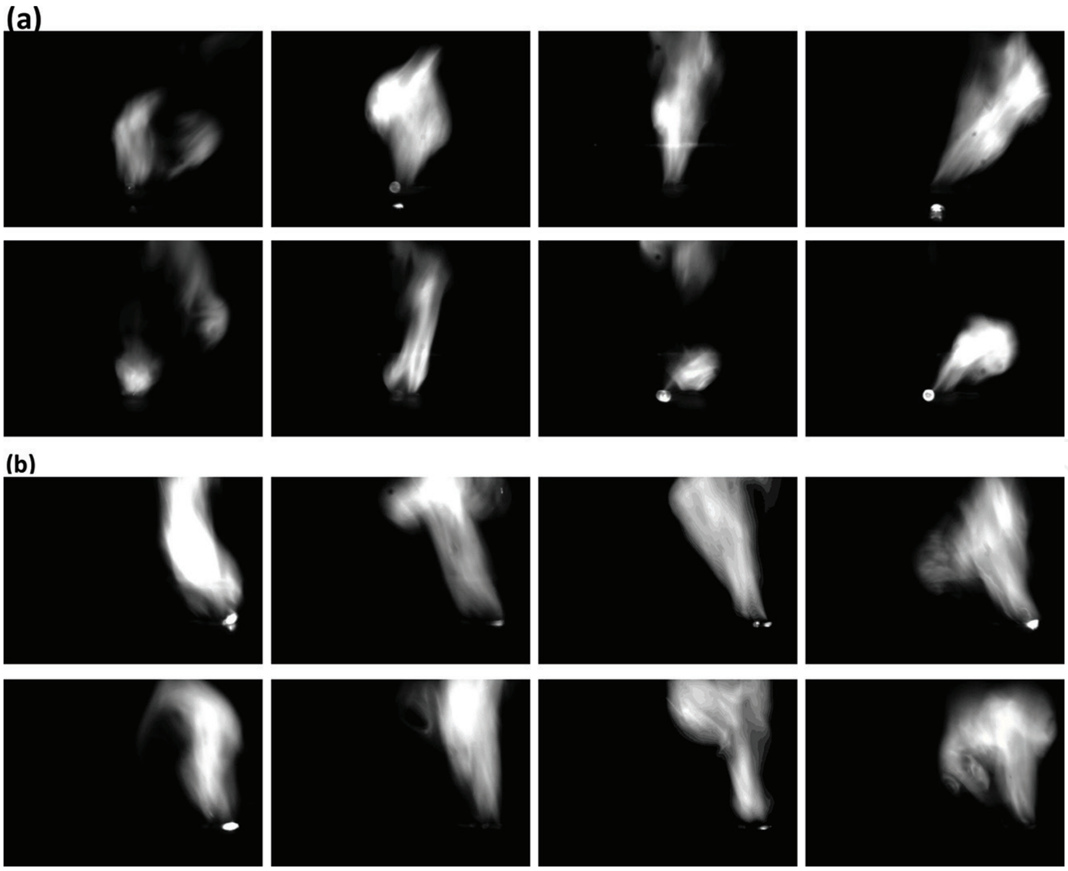

Figure 17. Images of laser-induced plasma plume captured during laser welding with laser power of 1000 W and welding speed of 30 mm/s with (a) single-beam laser, and (b) dual-beam laser with a 20:80 split beam energy ratio.

4.3. Nondestructive detection of defects using a spectrometer

4.3.1. Experimental setup

To observe the presence of pores, the weld bead had to be destructively sectioned in last two sections. In this part, spectroscopy is proposed as a nondestructive means to detect thepresence of pores in a lap joint configuration of a laser-welded AZ31B magnesium alloy as shown in **Figure 18**. The calculated electron temperature by the Boltzmann plot method was correlated to the presence of pores in the weld bead. Utilizing BeamView™ software, a CCD camera with a rate of 15 fps was also used in order to capture the intensity distribution of the laser-induced plasma. This device captures the intensity distribution in the laser and light sources.

In order to ensure that all conditions were the same for each run, the oxide layer was partially removed along the welding path, as schematically presented in **Figure 19**.

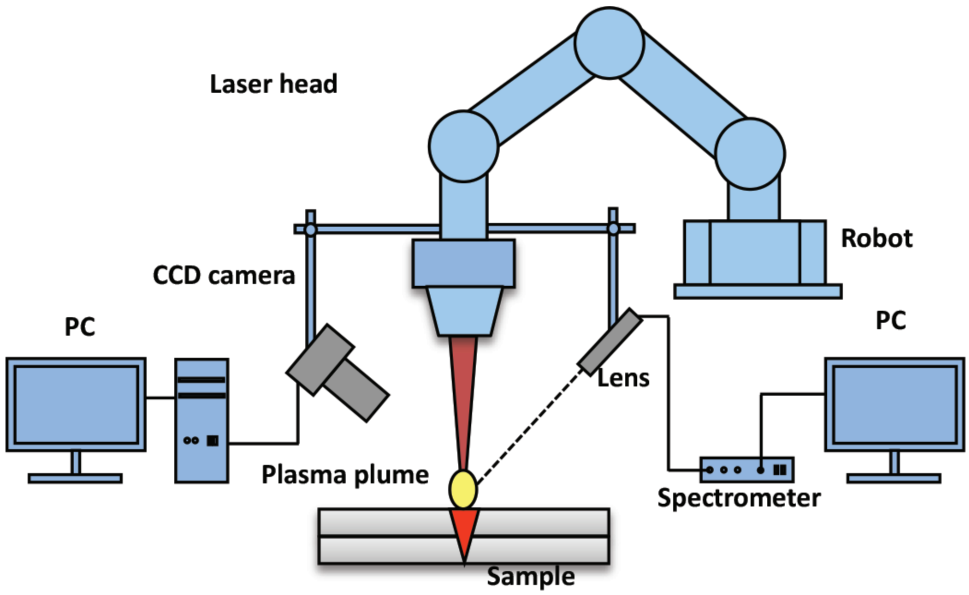

Figure 18. Schematic view of the laser welding process [15].

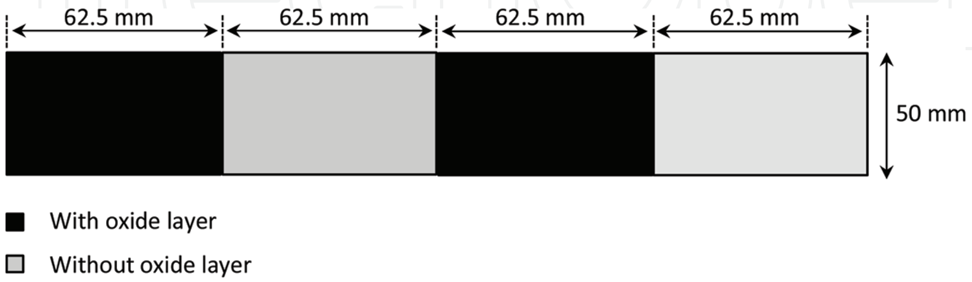

Figure 19. Schematic top view of partially removing the oxide layer on AZ31B magnesium alloy sheets.

In the laser welding process, a collision of free electrons in the plume region produces plasma that contains useful information, as discussed earlier. The plasma electron temperature can be calculated by the Boltzmann plot method. This method includes some important assumptions that should be considered prior to obtaining the final results. It is assumed that the laser-induced plasma with a homogeneous distribution should be optically thin and in local thermal equilibrium (LTE) for laser welding process [43]. By this assumption, the distribution of energy in the plasma region follows Maxwell's equation. Also the collision of particles is dominant to the radiation process [43–45]. The LTE assumption can be satisfied when the population of electrons in the unit volume is sufficiently high [43],

$$N_e \geq 1.6 \times 10^{12} T_e^{\frac{1}{2}} (\Delta E)^3 \ (\mathrm{cm}^{-3}) \tag{3}$$

where N_e is the electron density, T_e is electron temperature, and ΔE is the largest energy gap in the atomic energy level system. The integrated spectrum of emission-line intensities is given as [43],

$$\frac{N_n}{N_m} = \frac{g_n}{g_m} exp(-\frac{E_n - E_m}{kT}) \tag{4}$$

where g is the degeneracy, k is the Boltzmann constant, and E is the emitted energy. The electron temperature can be calculated for a chosen pair of emission lines by the following equation [43]:

$$T = \frac{E_{m_2} - E_{m_1}}{kLn(\frac{\omega_{m_2 n_2} A_{n_2 m_2} g_{m_2} R}{\omega_{m_1 n_1} A_{n_1 m_1} g_{m_1}})} \tag{5}$$

where R is the ratio of two populations.

By knowing the emission-line parameters, Eq. (5) can be applied to calculate the electron temperature of the laser-induced plasma. This method is advantageous because the calculations are relatively straightforward and can be easily implemented for the laser welding process. The upper energy levels for the selected emission lines, E_{m1} and, E_{m2} has to be satisfied by the following expression, $E_{m1} - E_{m2} > KT$ [47] (see **Table 4**).

Selected element	**Wavelength (nm)**	**Energy of the upper level (cm^{-1})**	**Statistical weight**	**Transition probability (S^{-1})**
Mg I	383.83	47957.027	5	4.03e7
Mg I	517.26	41197.403	3	3.37e7

Table 4. Spectroscopic information of selected elements [46].

4.3.2. Experimental results

The oxide layer is partially removed by a mechanical procedure prior to laser welding, as seen in **Figure 19**. As shown in this figure, one part is without an oxide layer followed by the part with the as-received oxide layer intact. **Figure 20** shows the top, bottom, and cross-sectional views of the weld bead achieved with laser power of 1200 W under two conditions: with and without an oxide layer.

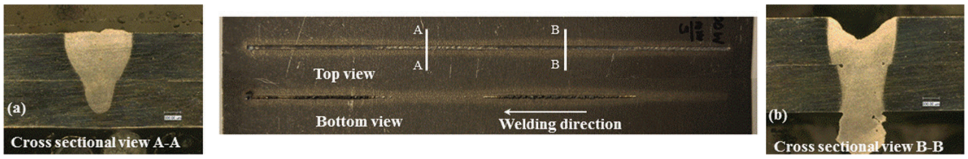

Figure 20. Top, bottom, and cross-sectional views of the weld with laser power of 1200 W for two different conditions at the faying surface of overlapped sheets (a) without oxide layer and (b) with oxide layer.

As clearly shown in **Figure 20**, there are discernable changes on weld bead, top and bottom view between two cases (with and without oxide layer). It is also clear that the presence of the oxide layer at the faying surface results in higher laser energy absorption that is discussed in detail in the work published by author [15] as well as Section 2.4.2. of this chapter.

The spectrum intensity of laser-induced plasma during the laser welding process is shown in **Figure 21**. Comparing the two cases regarding the presence of the oxide layer at the faying surface, it can be observed that the spectrum intensity is slightly less in the case with the oxide layer. As discussed earlier, the presence of the oxide layer at the interface had a dominant effect on the penetration depth. By considering the fact that the laser beam energy input to the metal sheets is constant, having greater penetration or a larger bead width means that more energy was absorbed by the metal and less was available to form a laser plume on top of the weld bead. The spectrum intensity for other laser parameters with more details could be found in the work that was done by authors [15].

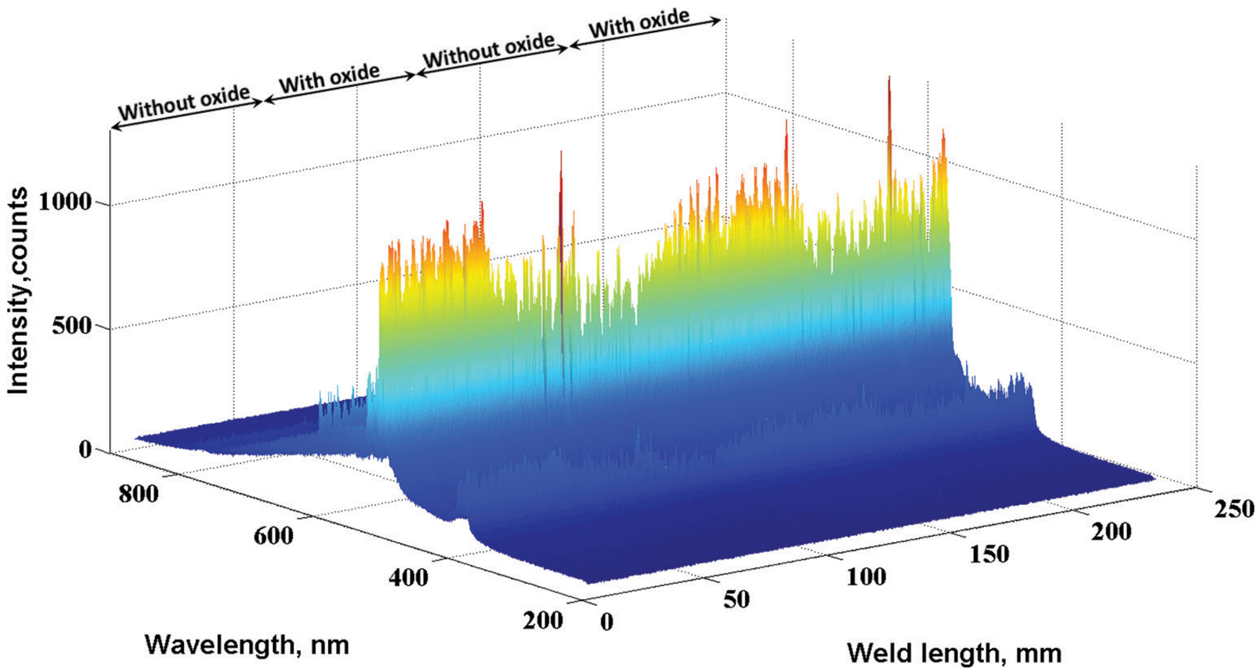

Figure 21. The spectrum intensity of laser induced plasma with laser power of 1200 W in the laser welding process.

In order to verify the intensity of the laser-induced plasma plume for the two surface conditions, with and without an oxide layer, a laser beam CCD device was used to view and capture images of the plasma plume in real time. This device is capable of capturing the intensity distribution images from almost any light or laser source. **Figure 22** shows the images captured during the laser welding of AZ31B magnesium alloy. **Figure 22(a)** and **(b)** presents the images of the plasma plume captured in the section without an oxide layer at the interface. **Figure 22(c)** and **(d)** shows the captured images of the plasma plume in the section with an oxide layer at the faying surface. As shown in this figure, the intensity is higher in the section without an oxide layer. This result confirms the recorded spectrum intensity results presented in **Figure 21**. The captured plasma plume images also revealed that the plasma plume is narrow and tall for the without-oxide section, although it is thicker and shorter for the section with an oxide layer. This result confirms that the laser-induced plasma plume was more stable during the welding of the section without an oxide layer.

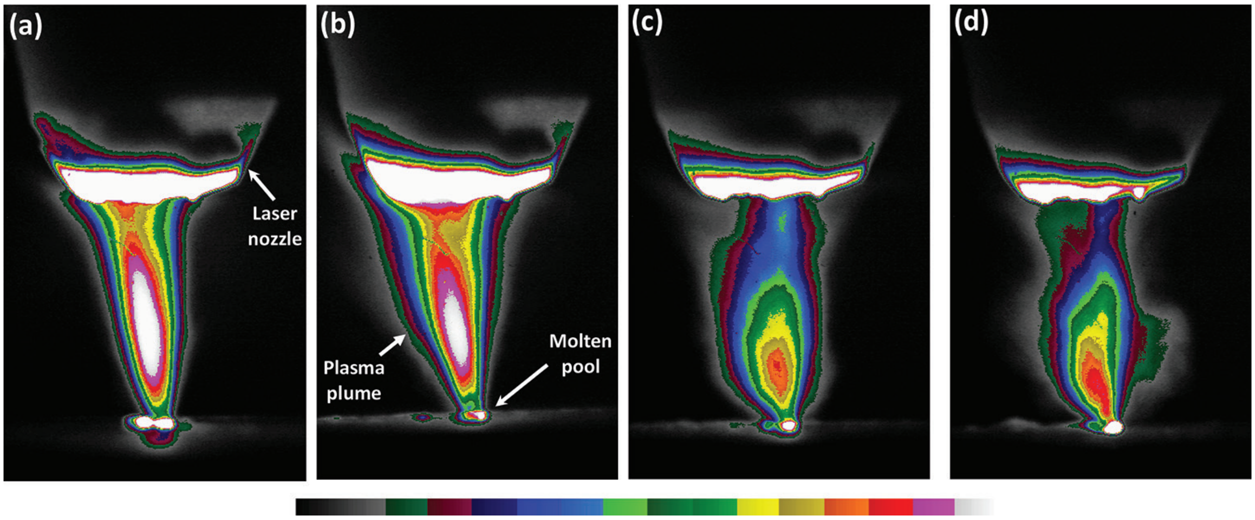

Figure 22. Captured images of laser induced plasma plume in real-time during laser welding with two surface conditions at the faying surface (a), and (b) without oxide layer, and (c), and (d) with oxide layer.

The calculated electron temperature from the spectrum intensity presented in **Figure 21** is shown in **Figure 23**. The electron temperature results exhibits varying levels and amounts of fluctuation along the weld bead. When the oxide layer is removed from the faying surface, the electron temperature shows a lower and uniform value with low fluctuation. The electron temperature shows a higher value with high fluctuation with an oxide layer at the faying surface. With an oxide layer at the faying surface, the keyhole is not stable due to the release of water molecules caused by magnesium hydroxide decomposition. This phenomenon was observed by a high-speed CCD camera, shown earlier in **Figure 3** of the work published previously by the authors [15]. When the keyhole is not stable, the formation of a plume and plasma at the top of the molten pool is not stable. In addition, the presence of spatters in the case with an oxide layer at the faying surface disturbs the plasma plume resulting in a decrease in the spectrum intensity (see **Figure 21**). These spatters increase the magnesium concentration in the plasma plume region causing a higher value for the electron temperature. This shows that basically there is a good correlation between pore formation in the weld bead and the calculated electron temperature.

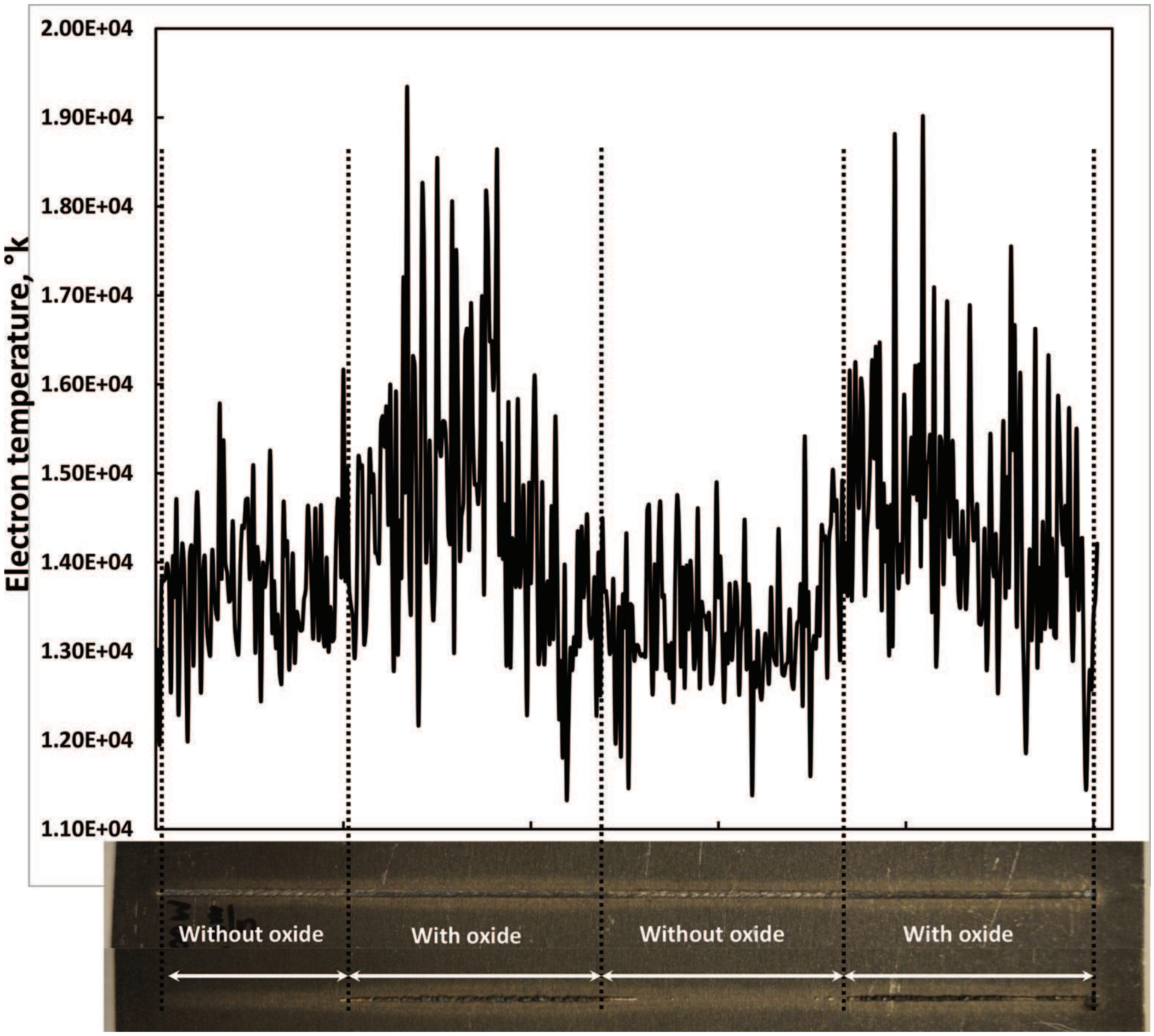

Figure 23. The calculated electron temperature for laser induced plasma with laser power of 1200 W.

4.4. Two-pass laser welding of magnesium alloy

From the earlier discussions, it is understood that welding as-received AZ31B magnesium alloys with a single-beam configuration results in pore formation in the weld bead (see **Figure 2**). In this section, a new method is introduced to use laser for preheating and welding. A defocused laser preheats the surface and in second pass, the focused laser beam welds two magnesium alloy sheets.

4.4.1. Experimental setup

The schematic view of two-pass experimental setup is shown in **Figure 24**. It can be seen that a larger defocused laser beam is applied to perform preheating before laser welding process. After that, a smaller focused beam is used to weld magnesium sheets (**Figure 24(b)**). The time between the first and second pass was about 10 s. **Table 5** shows the process parameters used in preheating and welding processes. The preheating parameter effect was evaluated on the weld quality. The laser welding power and speed were set at 1000 W and 30 mm/s which were used from authors' previous work [16].

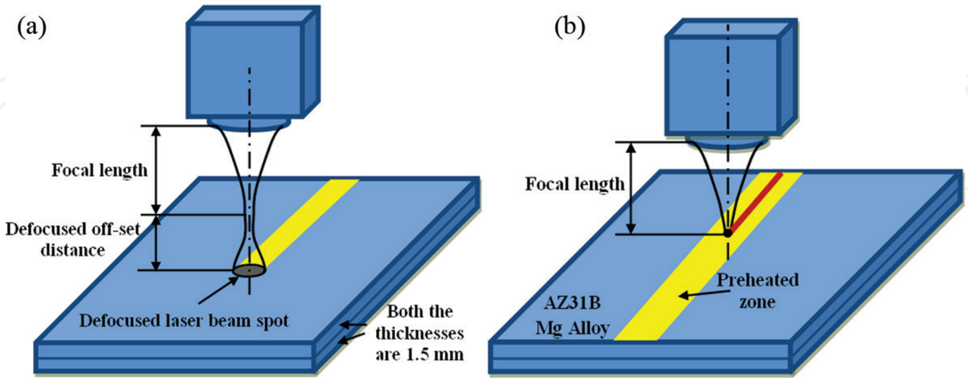

Figure 24. Two-pass laser welding process schematic view (a) preheating by a large defocused beam and (b) welding by a small focused beam.

	Preheating power (W)	Preheating speed (mm/s)	Focal distance (mm)	Laser welding power (W)	Laser welding speed (mm/s)
1	–	–	0	1000	30
2	2000	100	+40	1000	30
3	3000	100	+40	1000	30
4	2000	100	+35	1000	30
5	3000	100	+35	1000	30

Table 5. The preheating process parameters.

A spectrometer was employed also to study the laser induced plasma plume during the laser welding process as it was discussed in detail in Section. 2.3. The detected spectra was then used to calculate electron temperatures for the two different processes, two-pass laser welding (TPLW) and one-pass laser welding (OPLW). The electron temperature was used to compare the stability of the laser welding process for two experimental conditions. The spectrometer wavelength resolution was 0.4 nm, its integration time was 3 ms, and the slit width was 50 μm. The selected elements used as well as all equations for electron temperature calculation are as same as the one in Section 4.3.

4.4.2. Experimental results

Figure 25 presents the cross-sectional views of the welds. The laser power and welding speed (for either single pass or the second pass of a two-pass process) were the same for all cases, refer to **Table 5**. From observation of **Figure 25(a–d)**, it is clear that using an optimum preheating parameter set, a good quality of weld without pores can be achieved. These welds are achieved using a two-pass laser welding process with different power levels and focal distances. We had to make sure that the faying surface of the two overlapped sheets preheated effectively since this was the source of pore formation. As it can be seen in **Figure 25(c)**, pores are formed even though the preheating process was performed. This shows that to get a good weld quality, selecting optimum preheating parameters is critical. The viscosity of the molten magnesium is significantly low [6]. Therefore, when the weld bead was fully penetrated, the molten material dripped out at the bottom of two overlapped sheets caused pore formation. It can be observed from **Figures 25(a–d)** that when a higher preheating power is used, a shallower weld penetration was achieved. This can be discussed due to the difference between laser energy absorption on the surface magnesium alloy. The area of preheating between two overlapped sheets (upper sheet) is shown in **Figure 26**. The preheated region is lighter in color compared to its surrounding. Based on discussion in previous sections, the lighter area and non-preheated area (darker area) were assumed to be magnesium oxide (MgO)and magnesium hydroxide ($Mg(OH)_2$), respectively. Based on previous researches [48] magnesium hydroxide has a higher absorption coefficient in comparison to magnesium oxide [49]. Therefore, using a higher preheating laser power resulted in a greater rate of magnesium hydroxide decomposition at the faying surface. Then, this caused a lower level of power absorption leading to a less weld bead penetration. As a result, **Figure 25(a–d)** preheating with higher laser power resulted in less absorption in the second pass and a shallower penetration.

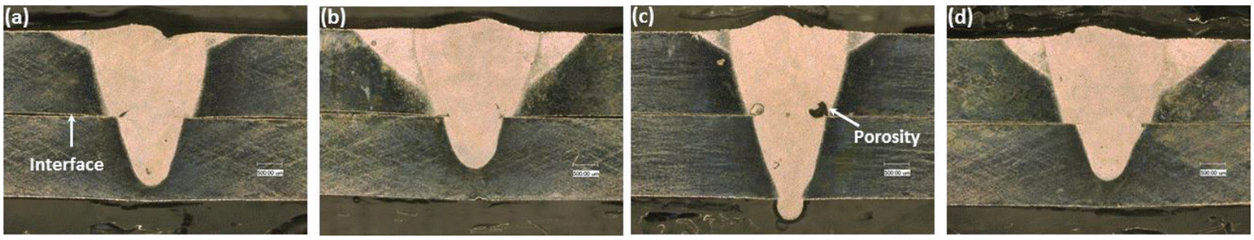

Figure 25. Polished cross-sectional views of magnesium sheet lap-shear laser welds. (a)–(d) Two-pass process with 1000 W and 30 mm/s welding parameters and preheat parameters of 100 mm/s and (a) 2000 W and 40 mm focal distance, (b) 3000 W and 40 mm focal distance, (c) 2000 W and 35 mm focal distance, and (d) 3000 W and 35 mm focal distance.

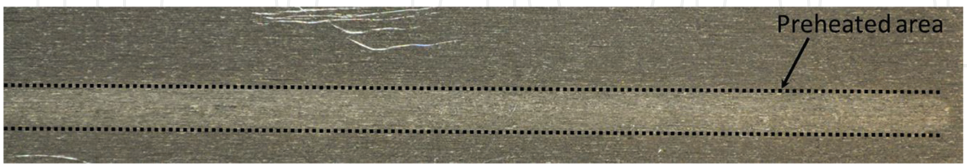

Figure 26. The preheated area with a lighter color on the upper sheet.

The top view of the two-pass samples acquired with different focal distances is displayed in **Figure 27**. The blowholes were seen in the sample that used less focal distance. The preheating process should not melt the substrate; however, when +20 mm focal distance was used, the energy density was high enough to melt substrate. As mentioned earlier, the viscosity and surface tension of molten magnesium is significantly low, which makes magnesium susceptible to weld defects like humping, or blowholes [6]. At a focal distance of +20 mm, due to higher level of preheating power, the mentioned properties of magnesium lead to have a low surface quality as shown in **Figure 27(b)**.

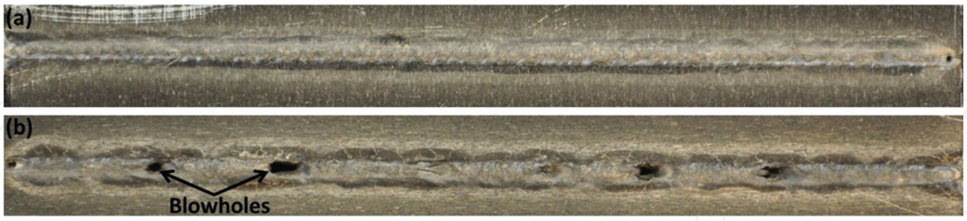

Figure 27. Comparison of focal distance: (a) +35 mm, and (b) +20 mm, and the effect it has upon the upper weld surface quality under the same preheating condition (3000 W, and 100 mm/s), laser power is 1000 W and welding speed is 30 mm/s.

The spectrum intensity from plasma plume single pass and two-pass welding processes is shown in **Figure 28**. Higher plasma plume intensity is achieved during the two-pass laser welding process (see **Figure 28(b)**). This can be due to a more stable plasma plume which can be resulted from a steadier welding condition which results in a higher weld quality. This stability was higher in two-pass compared to single pass. As discussed earlier, the stability is the result of optimum preheating which resulted in decomposition of magnesium hydroxide. Magnesium oxide (MgO) has a lower beam absorption that leads to higher plasma plume intensity since a greater amount of energy was available to form the plasma plume.

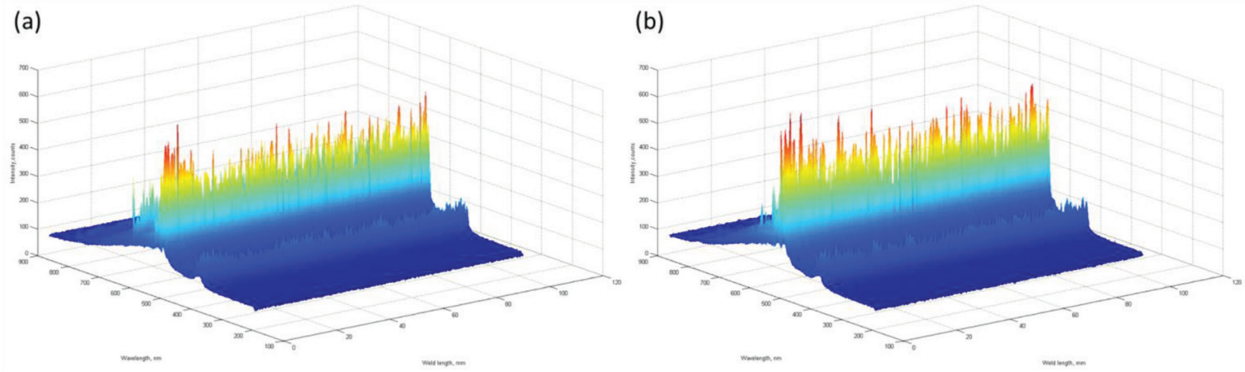

Figure 28. Laser-induced plasma intensity spectrum captured during laser welding under two conditions: (a) single pass and (b) two-pass laser welding.

The electron temperature was calculated for both the single pass and two-pass laser weld spectrum intensities as shown in **Figure 29**. The single pass laser welding process was less stable as expected and discussed in **Figure 25** which resulted in pore formation in the weld. The calculated electron temperature showed higher values when the single pass laser welding was performed. During the single pass laser welding process, the plasma plume intensity was affected by the release of hydrogen into the molten pool caused an unstable welding condition. This unstable condition advanced to the spatter formation as well as molten metal ejection from the molten pool. As also reported by other researchers [50], this can lead to an elevated level of concentration of molten metal in the plasma region leading to an increase in electron temperature. On the other hand, the electron temperature calculated from the two-pass laser welding process was lower. This reveals that the preheating was effective in releasing hydrogen gas prior to laser welding. This was resulted in a better stability in the weld. Less spatter formation and a more stable condition of the weld pool were both contributed to a lower electron temperature values in the two-pass laser welding process.

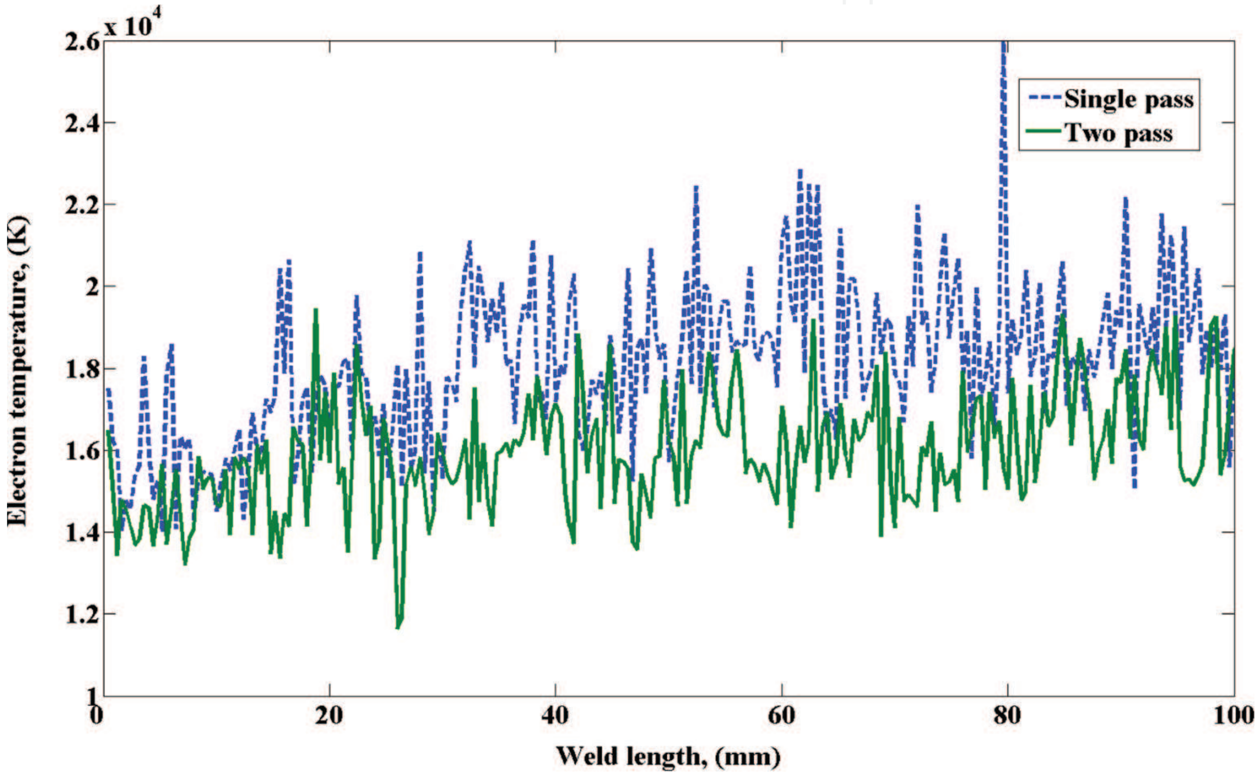

Figure 29. Calculated electron temperature during the laser welding process with different conditions: single pass and two pass.

To find out about the mechanical properties of the welds, tensile strength testing was performed on both single pass and two-pass laser welded sample groups. Five samples were cut for each group. The experimental results of lap-shear strength test are shown in **Figure 30**. The tensile load of was significantly greater for two-pass samples compared to the single pass laser welded samples. This shows that during the two-pass laser welding process, less pores are formed. Also, the greater variation in the as well as lower strength values both reveals that the single pass weld had less stable condition which was caused by release of hydrogen in molten pool as discussed earlier. Therefore, by performing an optimum preheating process during the two-pass welding process, pore formation could be effectively mitigated. More details about this study were published previously in earlier authors' work [17].

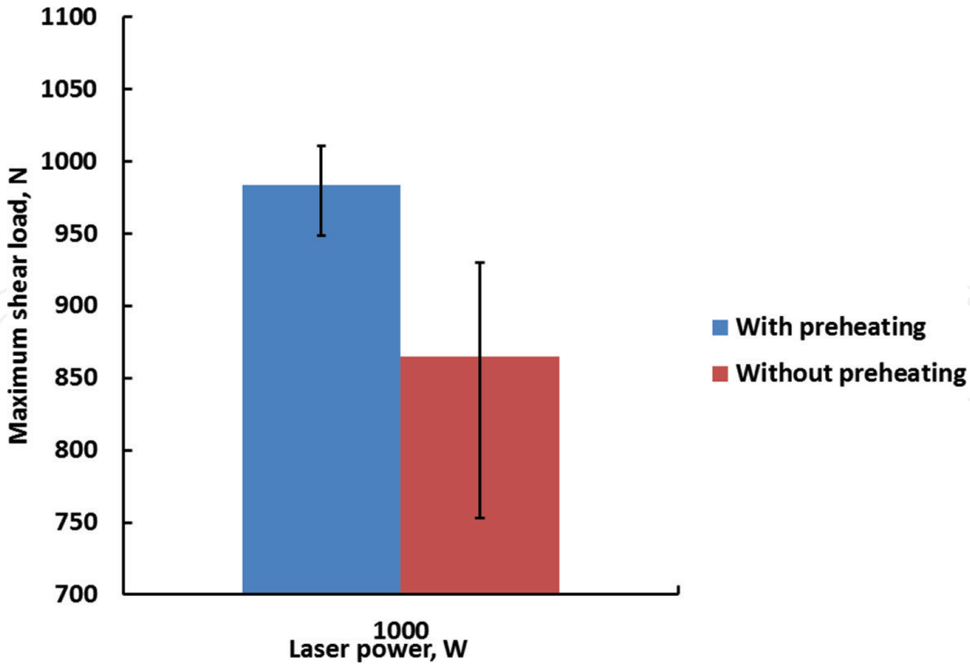

Figure 30. Average tensile shear load of laser welded AZ31 sheet in an overlap configuration with and without preheating.

5. Conclusions

(1) The as-received oxide layer on the surface of magnesium alloy causes pore formation in the weld bead, resulting from decomposition of the magnesium hydroxide at the faying surface of the two overlapped sheets. Pore formation could be mitigated effectively by introducing a plasma arc preheating source to decompose magnesium hydroxide prior to laser welding.

(2) Dual-beam laser welding with a 20:80 split beam energy ratio provides an improved weld bead quality with respect to porosity.

(3) The top surface quality of the weld bead obtained with dual-beam laser welding is smoother and more uniform than the quality obtained from single-beam laser welding as a result of less humping.

(4) The results of on-line monitoring the molten pool and laser-induced plasma plume revealed that the dual-beam laser welding is relatively more stable than single-beam laser welding.

(5) There was a good correlation between the calculated electron temperature detected from the laser-induced plasma and the presence of laser weld bead defects during the laser welding process.

(6) Two-pass laser welding mitigated pore formation in the weld bead. The calculated electron temperature is lower for two-pass laser welding compared to single pass laser welding indicating that the two-pass process is more stable.

Acknowledgements

This work was financially supported by the NSF's Grant No. IIP-1034652.

Author details

Masoud Harooni[1, 2, 3] and Radovan Kovacevic[1*]

*Address all correspondence to: kovacevi@smu.edu

1 Mechanical Engineering Department, Research Center for Advanced Manufacturing, Lyle School of Engineering, Southern Methodist University, Dallas, TX, USA

2 Keihin North America (Honda OEM), Greenfield, IN, USA

3 Center for Additive Manufacturing Research at IUPUI (CAMRI), Indiana University – Purdue University Indianapolis, Indianapolis, IN, USA

References

[1] Liu, L., Welding and joining of magnesium alloys, Woodhead Publishing, Cambridge, UK, 2010.

[2] Chowdhury, S.M., Chen, D.L., Bhole, S.D., Powidajko, E., Weckman, D.C., Zho, Y., (2011). microstructure and mechanical properties of fiber-laser-welded and diode-laser-welded AZ31 magnesium alloy. Metallurgical and Materials Transactions A 42: 1974–1989.

[3] Shrestha, S., (2010). Magnesium and surface engineering. Surface Engineering 26: 313–316.

[4] Blawert, C., Hort, N. and Kainer, K.U., (2004). The science, technology, and application of magnesium. Transactions of Indian Institute of Metals, Orlando, FL, USA, 57: 397–408.

[5] Yu, Z.H., Yan, H.G., Gong, X.S., Quan, Y.J., Chen, J.H., Chen, Q., (2009). Microstructure and mechanical properties of laser welded wrought ZK21 magnesium alloy. Materials Science and Engineering A 523: 220–225.

[6] Cao, X., Jahazi, M., Immarigeon, J.P., Wallace, W., (2006). A review of laser welding techniques for magnesium alloys. Journal of Materials Processing Technology 171: 188–204.

[7] Gao, M., Tang, H.G., Chen, X.F., and Zeng, X.Y., (2012). High power fiber laser arc hybrid welding of AZ31B magnesium alloy. Materials and Design 42: 46–54.

[8] Cao, X., and Jahazi, M., (2009). Effect of welding speed on the quality of friction stir welded butt joints of a magnesium alloy. Materials and Design 30(6): 2033–2042.

[9] Shi, H., Qiu, R., Zhu, J., Zhang, K., Yu, H., and Ding, G., (2010). Effects of welding parameters on the characteristics of magnesium alloy joint welded by resistance spot welding with cover plates. Materials and Design 31: 4853–4857.

[10] Berlin, A., Nguyen, T.C., Worswick, M.J., Zhou, Y., (2011). Metallurgical analysis of magnetic pulse welds of AZ31 magnesium alloy. Science and Technology of Welding and Joining 16: 728–734.

[11] Harooni, M., Kong, F., Carlson, B., Kovacevic, R., (2012). Mitigation of pore generation in laser welding of magnesium alloy AZ31B in lap joint configuration. ASME International Mechanical Engineering Congress & Exposition, Houston, TX.

[12] Harooni, M., Kong, F., Carlson, B., and Kovacevic, R., (2012). Studying the effect of laser welding parameters on the quality of ZEK100 magnesium alloy sheets in lap joint configuration. International Congress on Applications of Lasers & Electro-Optics (ICALEO), Anaheim, CA.

[13] Harooni, M., Carlson, B., and Kovacevic, R., (2013). Effect of process parameters on the weld quality in laser welding of AZ31B magnesium alloy in lap joint configuration, International Congress on Applications of Lasers & Electro-Optics (ICALEO), Miami, FL.

[14] Harooni, M., Blair, C., Kovacevic, R., (2014). Dual-beam laser welding of AZ31B magnesium alloy in zero-gap lap joint configuration. Optics and Laser Technology 56: 247–255.

[15] Harooni, M., Carlson, B., and Kovacevic, R., (2014). Detection of defects in laser welding of AZ31B magnesium alloy in zero-gap lap joint configuration by a real-time spectroscopic analysis. Optics and Lasers in Engineering 56, 54–66.

[16] Harooni, M., Carlson, B., and Kovacevic, R., (2014). Pore formation mechanism and its mitigation in laser welding of AZ31B magnesium alloy in lap joint configuration. Materials and Design 58, 265–276.

[17] Harooni, M., Ma, J., Carlson, B., and Kovacevic, R., (2015). Two-pass laser welding of AZ31B magnesium alloy. Journal of Materials Processing Technology 216, 114–122.

[18] Harooni, M., Experimental and numerical studies on the issues in laser welding of light-weight alloys in a zero-gap lap joint configuration. PhD thesis, Southern Methodist University, Dallas, TX, USA, 2014.

[19] Mikucki, B.A., and Shearouse, J.D., (1993). Interdependence of hydrogen and microporosity in magnesium alloy AZ91. Proceedings of Magnesium Properties and Applications for Automobile, Detroit, MI.

[20] Katayama, S., Seto, N., Kim, J.D., Matsunawa, A., (1998). Formation mechanism and suppression procedure of porosity in high power laser welding of aluminum alloys. Laser Institute of America, ICALEO, Orlando, FL.

[21] Liu, L., Song, G., Liang, G., and Wang, J., (2005). Pore formation during hybrid laser-tungsten inert gas arc welding of magnesium alloy AZ31B—mechanism and remedy. Materials Science and Engineering: A 390, 76–80.

[22] Pastor, M., Zhao, H., Martukanitz, R.P., Debroy, T., (1999). Porosity, underfill and magnesium loss during continuous wave Nd:YAG laser welding of thin plates of aluminum alloys 5182 and 5754. Welding Journal 78: 207s–216s.

[23] Zhao, H. and Debroy, T., (2001). Pore formation during laser beam welding of die cast magnesium alloy AM60B—mechanism and remedy. Welding Journal 80: 204s–210s.

[24] Matsunawa, A., Kim, J.D., Mizutani, M., Katayama, S., (1998). Dynamics of keyhole and molten pool in laser welding. Journal of Laser Applications 10: 247–254.

[25] AHC Surface Coating [Online]. Available: https://www.ahc-surface.com/en/surface-treatment/processes/magoxid-coat. [Accessed 27 June 2016].

[26] Keronite [Online]. Available: http://www.keronite.com/. [Accessed 27 June 2016].

[27] Tagnite [Online]. Available: http://www.tagnite.com/tagnite_coating/. [Accessed 27 June 2016].

[28] Zhu, J., Li, L., and Liu, Zh., (2005). CO_2 and diode laser welding of AZ31 magnesium alloy. Applied Surface Science 247: 300–306.

[29] Marya, M. and Edwards, G.R., (2000). The laser welding of magnesium alloy AZ91. Welding in the World 44: 31–37.

[30] Powidajko, E.J.M., Weldability of AZ31B magnesium sheets by laser welding processes. PhD thesis, University of Waterloo, Waterloo, Canada, 2009.

[31] Pilling, N.B., and Bedworth, R.E., (1923). The oxidation of metals at high temperatures. Journal of Institute of Metals 29: 529–591.

[32] Wegrzyna, J., Mazurb, M., Szymańskib A., and Balcerowskab B., (1987). Development of a filler for welding magnesium alloy GA8. Welding International 1: 146–150.

[33] Liu, L.M., Ren, D.X., (2010). Effect of adhesive on molten pool structure and penetration in laser weld bonding of magnesium alloy. Optics and Lasers in Engineering 48: 882–887.

[34] Otsuki, S., Fukuzawa, S., (2004). Organic electroluminescent device and method for fabricating same. U.S. patent 6737176.

[35] Wakelin, S., (2007). System and method for getting gas-phase contaminants within a sealed enclosure. U.S. patent 7160368.

[36] Fournier, V., Marcus, P., and Olefjord, I., (2002). Oxidation of magnesium. Surface and Interface Analysis 34: 494–497.

[37] Kuroda, Y., Yasugi, E., Aoi, H., Miura, K., Morimoto, T., (1988). Interaction of water with the surface of magnesium oxide. Journal of the Chemical Society, Faraday Transactions: Physical Chemistry in Condensed Phases 84: 2421–2430.

[38] Halikia, I., Neou-Syngouna P., and Kolitsa D., (1998). Isothermal kinetic analysis of the thermal decomposition of magnesium hydroxide using thermogravimetric data. Thermochimica Acta 320: 75–88.

[39] Pavelic V., Tanbakuchi, R., Uyehara, O.A., Myers, P.S., (1969). Experimental and computed temperature histories in gas tungsten arc welding of thin plates. Welding Journal Research Supplement 48: 295s–305s.

[40] Haboudou, A., Peyre, P., Vannes, A., and Peix, G., (2003). Reduction of porosity content generated during Nd:YAG laser welding of A356 and AA5083 aluminium alloys. Materials Science and Engineering A 363, 40–52.

[41] Ready, J.F., (2001). LIA handbook of laser materials processing. Laser Institute of America Orlando, FL, USA.

[42] Xie, J., (2002). Dual beam laser welding. Welding Journal 81: 223s–230s.

[43] Griem, H.R., (1997). Principles of plasma spectroscopy. Cambridge University Press, Cambridge, UK.

[44] Liu, L. and Hao, X., (2008). Study of the effect of low-power pulse laser on arc plasma and magnesium alloy target in hybrid welding by spectral diagnosis technique. Journal of Physics D: Applied Physics, 41, 1–10.

[45] Rizzi, D., Sibillano, T., Calabresa, P.P., Ancona, A. and Lugara, P.M., (2011). Spectroscopic, energetic and metallographic investigations of the laser lap welding of AISI 304 using the response surface methodology. Optics and Lasers in Engineering 49: 892–898.

[46] NIST Atomic Spectra Database [Online]. Available: http://www.nist.gov/pml/data/asd.cfm. [Accessed 01 February 2013].

[47] Lacroix, D., Jeandel, G., and Boudot, C., (1997). Spectroscopic characterization of laser induced plasma created during welding with a pulsed Nd: YAG laser. Journal of Physics D: Applied Physics, 81: 6599–6606.

[48] Ren, D., Liu, L., and Li, Y., (2012). Investigation on overlap joining of AZ61 magnesium alloy: laser welding, adhesive bonding, and laser weld bonding. International Journal of Advanced Manufacturing Technology 61(1–4): pp. 195–204.

[49] Magnesium oxide (MgO), Crystran [Online]. Available: http://www.crystran.co.uk/optical-materials/magnesium-oxide-mgo. [Accessed 5 March 2014].

[50] Kong, F., Ma, J., Carlson, B., Kovacevic, R., (2012). Real-time monitoring of laser welding of galvanized high strength steel in lap joint configuration. Optics and Laser Technology 44: 2186–2196.

IntechOpen